

AD-A160 392

ATMOSPHERIC MULTIPATH PROPAGATION OVER A LONG
TERRESTRIAL LINE-OF-SIGHT PATH(U) ROME AIR DEVELOPMENT
CENTER GRIFFISS AFB NY U H LAMMERS ET AL. APR 85

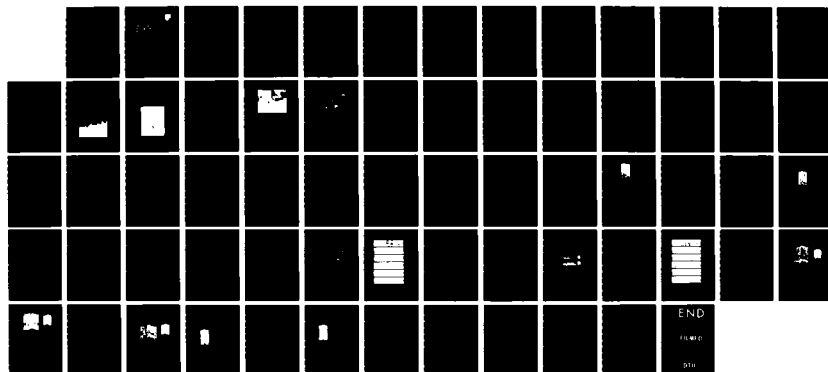
UNCLASSIFIED

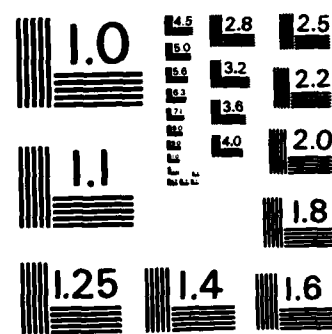
RAFD-TR-85-79

1/1

F/G 17/2.1

NL





MICROCOPY RESOLUTION TEST CHART
NATIONAL BUREAU OF STANDARDS - 1963 - A

12

RADC-TR-85-79
In-House Report
April 1985



ATMOSPHERIC MULTIPATH PROPAGATION OVER A LONG TERRESTRIAL LINE-OF-SIGHT PATH

AD-A160 392

Uwe H. W. Lammers
Richard A. Marr

APPROVED FOR PUBLIC RELEASE; DISTRIBUTION UNLIMITED

DTIC ELECTE
OCT 17 1985
S D
B

DTIC FILE COPY

ROME AIR DEVELOPMENT CENTER
Air Force Systems Command
Griffiss Air Force Base, NY 13441-5700

This report has been reviewed by the RADC Public Affairs Office (PA) and is releasable to the National Technical Information Service (NTIS). At NTIS it will be releasable to the general public, including foreign nations.

RADC-TR-85-79 has been reviewed and is approved for publication.

APPROVED:



TERENCE J. ELKINS
Chief, Propagation Branch
Electromagnetic Sciences Division

APPROVED:



ALLAN C. SCHELL
Chief, Electromagnetic Sciences Division

FOR THE COMMANDER:



JOHN A. RITZ
Acting Chief, Plans Office

If your address has changed or if you wish to be removed from the RADC mailing list, or if the addressee is no longer employed by your organization, please notify RADC (EEP) Hanscom AFB MA 01731. This will assist us in maintaining a current mailing list.

Do not return copies of this report unless contractual obligations or notices on a specific document requires that it be returned.

Unclassified

SECURITY CLASSIFICATION OF THIS PAGE

REPORT DOCUMENTATION PAGE

1a. REPORT SECURITY CLASSIFICATION Unclassified		1b. RESTRICTIVE MARKINGS											
2a. SECURITY CLASSIFICATION AUTHORITY		3. DISTRIBUTION/AVAILABILITY OF REPORT											
2b. DECLASSIFICATION/DOWNGRADING SCHEDULE		Approved for public release; Distribution unlimited.											
4. PERFORMING ORGANIZATION REPORT NUMBER(S) RADC-TR-85-79		5. MONITORING ORGANIZATION REPORT NUMBER(S)											
6a. NAME OF PERFORMING ORGANIZATION Rome Air Development Center	6b. OFFICE SYMBOL (If applicable) EEP	7a. NAME OF MONITORING ORGANIZATION Rome Air Development Center											
8a. ADDRESS (City, State and ZIP Code) Hanscom AFB Massachusetts 01731		7b. ADDRESS (City, State and ZIP Code) Hanscom AFB Massachusetts 01731											
8c. NAME OF FUNDING/SPONSORING ORGANIZATION	8d. OFFICE SYMBOL (If applicable)	9. PROCUREMENT INSTRUMENT IDENTIFICATION NUMBER											
8e. ADDRESS (City, State and ZIP Code)		10. SOURCE OF FUNDING NOS.											
11. TITLE (Include Security Classification) Atmospheric Multipath Propagation (Contd)		PROGRAM ELEMENT NO. 62702F	PROJECT NO. 4600	TASK NO. 16	WORK UNIT NO. 07								
12. PERSONAL AUTHOR(S) Uve H. W. Lammers and Richard A. Marr													
13a. TYPE OF REPORT Scientific	13b. TIME COVERED FROM _____ TO _____	14. DATE OF REPORT (Yr., Mo., Day) 1985 April		15. PAGE COUNT 64									
16. SUPPLEMENTARY NOTATION													
17. COSATI CODES <table border="1"><tr><td>FIELD</td><td>GROUP</td><td>SUB. GR.</td></tr><tr><td>09</td><td>17</td><td>02. 1</td></tr><tr><td> </td><td> </td><td> </td></tr></table>	FIELD	GROUP	SUB. GR.	09	17	02. 1				18. SUBJECT TERMS (Continue on reverse if necessary and identify by block number) Microwave line-of-sight propagation, Refractive bending Multipath angle-of-arrival Multipath delay			
FIELD	GROUP	SUB. GR.											
09	17	02. 1											
19. ABSTRACT (Continue on reverse if necessary and identify by block number) Measurements of atmospheric multipath propagation were conducted over an 87.6-km test path in the New England area. Characteristic of this program are (a) the pathlength and its potential for propagation effects not normally found on shorter commercial communication links and (b) an effort to explore the propagation mechanism through coordinated measurements of meteorological and wave parameters. The height difference of 178.6 m between transmitting and receiving antennas was the lowest available to retain line-of-sight clearance at this pathlength and yet produce maximum interaction with stratified regions of enhanced refractivity gradient. Radiosonde derived refractivity profiles were obtained at several locations along the test path when propagation conditions warranted this. Dual receiving systems measured multiple wavefront angles of arrival and delay differences. A 29-ft antenna, continuously scanning in elevation, provided angular patterns with 0.15° resolution at the operating frequency of 15.84 GHz. A second, spaced antenna of 3-ft diameter													
20. DISTRIBUTION/AVAILABILITY OF ABSTRACT UNCLASSIFIED/UNLIMITED <input checked="" type="checkbox"/> SAME AS RPT. <input type="checkbox"/> DTIC USERS <input type="checkbox"/>		21. ABSTRACT SECURITY CLASSIFICATION Unclassified											
22a. NAME OF RESPONSIBLE INDIVIDUAL Uve H. W. Lammers		22b. TELEPHONE NUMBER (Include Area Code) (617) 861-4239	22c. OFFICE SYMBOL EEP										

DD FORM 1473, 83 APR

EDITION OF 1 JAN 73 IS OBSOLETE.

Unclassified
SECURITY CLASSIFICATION OF THIS PAGE

Unclassified

SECURITY CLASSIFICATION OF THIS PAGE

11. (Contd)

Over a Long Terrestrial Line-of-Sight Path

19. (Contd)

and fixed-pointed was connected to a delay scanning receiver, performing a correlation analysis on the 400 Mb/sec PRN modulation. Radio data were taken on a total of 74 days spanning the summer and fall months of 1983 when multipath interference is most probable in New England. Meteorological data collection, covering 21 of these days, was prompted by either forecast or actual radio observation. A subset of 11 days shows both multipath propagation and meteorologically verified ducting layers. We outline experimental systems and procedures. Computer modeling of the wave propagation mechanism and simulation of angle-of-arrival and delay scans are used to interpret the experimental observations of 1 November 1983, a typical day of severe refractive disturbance.

Unclassified

SECURITY CLASSIFICATION OF THIS PAGE

Preface

The cooperation of the Tropospheric Structure Branch, Air Force Geophysics Laboratory, has been an important factor in this work.

The authors are indebted to Dr. D. Hayes and Mr. M. Sowa for their help during early phases of radio data collection.

Operation of the Saddleback Mountain transmitter was kindly supported by New Hampshire Public Television engineering personnel.



Accession #	77
ATIS	100
DATE	10/10/77
TIME	10:00
JO	100
RY	100
Dist	100
Availability Sec 3	
Dist	100
Availability Sec 3	
A	100

A large checkmark is present in the top right corner of the form.

Contents

1. INTRODUCTION	1
2. PROPAGATION EXPERIMENT	3
2.1 Microwave Systems	3
2.2 Experimental Path	8
2.3 Meteorological Sounding	13
3. PROPAGATION ANALYSIS	18
3.1 Model Calculation	19
3.2 Scan Simulation	24
3.3 Test Case	27
3.4 Sub-Resolution Effects	33
4. MULTIPATH DATA INTERPRETATION	36
4.1 Delay Resolution Test	36
4.2 Overview of 1 November 1983 Data	38
4.3 Multipath Angular Events	45
4.4 Multipath Delay Events	49
5. CONCLUSIONS	53
REFERENCES	55

Illustrations

1. AOA/TOA System Block Diagram	4
2. Transmitter Site on Saddleback Mountain	6
3. AOA and TOA Receiving Antennas at Prospect Hill	7
4. Receiving and Data Recording Equipment at Prospect Hill	9
5. Saddleback Mountain to Prospect Hill Path	10
6. Saddleback Mountain to Prospect Hill Terrain Profile	10
7. Terrain Reflected and Direct Ray Elevation Angles vs k-Factor	12
8. Height Regions With Ducting Gradients vs Launch Positions Along Path and Launch Times	17
9. Three-Ray Multipath vs Layer Height	19
10. Computed Multipath Angles of Arrival	20
11. Computed Multipath Delays	21
12. Computed Ray Penetration Depth Into Ducting Layer	22
13. Minimum Layer Depth for Multipath Propagation	23
14. Length of Ray Path in Ducting Layer	24
15. Simulated Angle-of-Arrival Scan	25
16. Simulated Time-of-Arrival Scan	27
17. Simulation of Multipath Structure Due to Rising Ducting Layer as Resolved by AOA System	29
18. Simulation of Multipath Structure Due to Rising Ducting Layer as Resolved by TOA System	32
19. TOA Two-Signal Sub-Resolution Interaction	34
20. Experimental Delay Scans	38
21. Received Signal Level vs Elevation Angle on 1 November 1983	39
22. AOA and TOA Scan Amplitudes During and After Multipath Episode on 1 November 1983	42
23. Received Signal Level vs Delay on 1 November 1983	44
24. AOA Scan Sequence on 1 November 1983 Based on Amplitude Change	46
25. AOA Scan Sequence on 1 November 1983 Based on Phase and Angle Changes	47
26. AOA Scan Sequence on 1 November 1983 Based on Phase Change	49
27. TOA Scan Sequence on 1 November 1983 Based on Two-Component Multipath	50
28. TOA Scan Sequence on 1 November 1983 Based on Three-Component Multipath	52

Tables

1. Duct Parameters on Selected 1983 Days	15
2. Parameters Used in Elevation Beam Model	25
3. Parameters Used in Correlator Model	27
4. Refractivity Change and Refractivity Gradient Between Transmitter and Receiver Heights on 1 November 1983	41

Atmospheric Multipath Propagation Over a Long Terrestrial Line-of-Sight Path

1. INTRODUCTION

Under suitable conditions, superrefractive layers in the troposphere provide signal propagation paths in addition to the direct path between line-of-sight (LOS) microwave terminals. The multiple signals arriving at the receiving antenna have wavefronts differing both in vertical inclination and in path delay. Wavefront tilt at the receiving aperture is a function of the exact path that the wave travels which in turn is dependent on the refractivity gradient at each point along the way. Differences between the inclination of various multipath wavefronts do not exceed one degree under most conditions. Traveling along trajectories of unequal length, individual multipath wavefronts arrive at the receiver with differences in path delay. In addition to the pathlength, the propagation velocity at each point along the way, which is a function of the refractivity at that point, determines the arrival time of a particular wave. Typically, delay differences range up to several nanoseconds, although tens of nanoseconds are conceivable.

Under multipath propagation conditions the receiver input is a phasor sum with each component signal weighted by the antenna gain in its direction of arrival. Specific combinations of component signal amplitudes and phases lead to partial or complete cancellation of the sum signal. For a narrowband communication system, cancellation occurs more or less uniformly across the transmitted spectrum, causing

(Received for publication 26 April 1985)

outages due to loss of signal. For a wideband communication system, portions of the transmitted spectrum are affected differently, leading to outages from signal distortion rather than signal loss. Frequency and height diversity offer means to mitigate cancellation in a narrowband system. Wideband systems often cannot benefit from such techniques, since they only transpose distortions from one part of the occupied spectrum to another. Adaptive signal processing is used instead to alleviate multipath interference. Actually, the multipath structure's inherent diversity is used to improve performance.¹

Angle diversity is under consideration as a technique independent of signal bandwidth to counteract multipath effects on LOS links.² Elevation angle differences between wavefronts are small enough to require the use of a large receiving aperture, in order to discriminate against all but one signal component. Elevation angle tracking is likely to be necessary.³ Alternatively, the sum and difference patterns of a fixed-pointing conventional-size monopulse antenna provide signals for a simple form of angle diversity.

Many experiments have been conducted and theoretical models designed to explain and quantify the tropospheric multipath propagation phenomenon. The present effort has three specific objectives:

(1) Most commercial LOS communication links are of relatively short length. An early model⁴ suggested a third-order delay spread dependence on range. Measured data from short links agreed. For the longer Air Force LOS links such as the ones found in Europe this would have meant excessive delay spreads which had to be proved or disproved experimentally. Parl's recent model⁵ leads to a third-order dependence for short distances only and predicts a linear relationship at greater distances. This is confirmed by Sasaki and Akiyama⁶ who supplement their theoretical calculations with some measured data from five paths ranging between 23.2 and 78.6 km in length. A wide variability in their path geometries appears to mask the linear range dependence. No excessive delay spreads were found on the longer paths.

(2) A large number of inferences on LOS multipath mechanisms are drawn from spectral and temporal measurements on actual communication links. Some experiments, probing the physics of wave propagation more directly, suffer from limitations inherent in the measurement techniques used. Thus, with frequency-swept or interferometric systems it becomes progressively more difficult to resolve amplitudes, angle-of-arrival (AOA) differences, and time-of-arrival (TOA) differences when more than two phasors contribute to the received signal. In our investigations we alleviated these difficulties to some extent by resolving multiple

(Due to the large number of references cited above, they will not be listed here. See References, page 55.)

wavefronts with a narrow pencil beam in elevation angle and with a high bit rate digital modulation in differential delay.

(3) The interpretation of signals received in microwave propagation experiments is often hampered by extremely limited meteorological information. Although the spatial refractivity structure is difficult to probe to the detail to which it affects wave propagation, we did at least sample vertical profiles at several points along the path during periods of predicted or observed multipath conditions.

2. PROPAGATION EXPERIMENT

Data were obtained during the 1982 and 1983 summer and fall seasons of greatest ducting probability in New England. The 1982 test path of 73.1 km length from Pack Monadnock near Peterborough, NH to Prospect Hill, Waltham, MA exhibited a height difference of 439.5 m between terminals. This geometry was less conducive to multipath effects than the geometry of the 1983 test path from Saddleback Mountain near Deerfield, NH to Prospect Hill. The height difference on the Saddleback Mountain path of 87.6-km length was 178.6 m. The report addresses measurements obtained on the latter path. Data were jointly collected by the Meteorology Laboratory of the Air Force Geophysics Laboratory who probed the refractivity structure with balloon-borne instrumentation, and by the Electromagnetic Sciences Division of RADC who was responsible for the design and operation of the microwave links.

2.1 Microwave Systems

At the Prospect Hill Field Station the Air Force owns a 29-ft fully steerable Cassegrain antenna which was chosen as the receiving antenna for the AOA measurement system. This antenna is usable well into the millimeter wavelength region. K_u-band equipment was on hand that could be modified to serve the intended purpose. Since path attenuation due to precipitation is of no concern in this context, and since refractive bending and propagation velocity are largely independent of frequency in the microwave range, all measurements were conducted at $f = 15.84$ GHz. A 3-dB beamwidth of 0.15° at this frequency is compatible with the 1°-range or so, over which multiple components can be expected.

The block diagram in Figure 1 shows the basic elements of the dual AOA/TOA measurement system. The transmitter is common to both. The 15.84-GHz carrier is derived through frequency multiplication from the 5-MHz output of a Cesium beam frequency standard. The same source drives the 400 Mb/sec pseudorandom noise (PRN) generator. The PRN wordlength is 1023 bits. The carrier is biphasic modulated with the PRN sequence in a doubly balanced mixer. After amplification, the signal is transmitted by a 3-ft parabolic antenna. At 15.84 GHz, the

3-dB elevation beamwidth of this antenna is 1.45° , so that multipath components should be attenuated by a decibel or less in most cases, if the antenna is aligned appropriately. A carrier feedthrough of the order of -15 dB can be expected in a doubly balanced mixer when compared with the power contained in the modulation sidebands. This fact is taken advantage of in the AOA system whose narrowband receiver is tuned to the transmitted rest carrier. The transmit power advantage of 15 dB that the TOA system has over the AOA system is more than compensated for by the gain of the respective receiving antennas. The TOA receiving antenna is another 3-ft parabolic dish. The transmitter operates at a total output level of 100 mW.

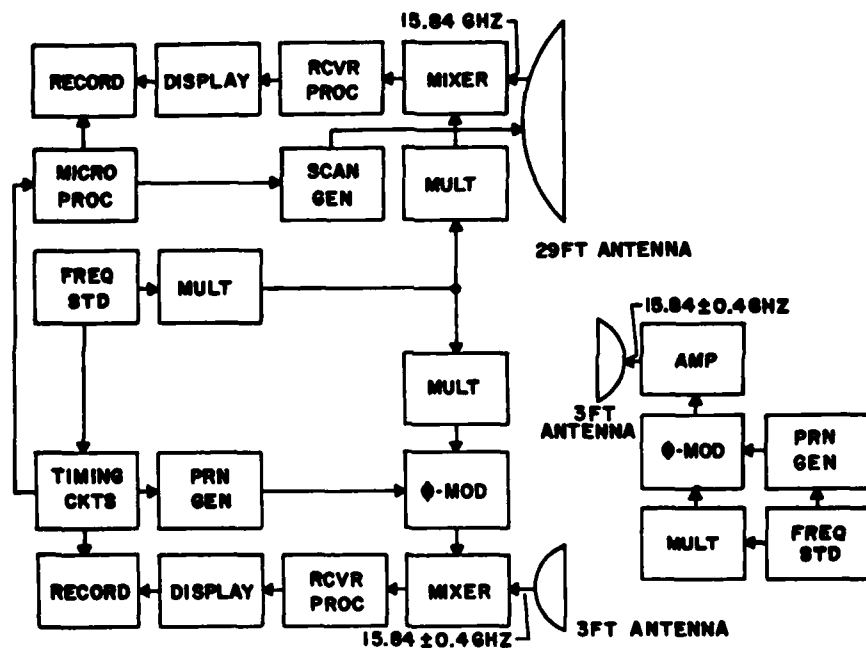


Figure 1. AOA/TOA System Block Diagram

The AOA and TOA receivers use a quadruple conversion scheme. They are essentially identical with the exception of a first local oscillator in the TOA receiver which is biphasic modulated with a locally generated replica of the 400 Mb/sec transmitted PRN sequence. When the locally generated phase modulation is synchronous with the one transmitted and delayed via the direct or indirect paths, the output from the first TOA receiver mixer is a narrowband signal similar to that from the

AOA receiver. After narrowband filtering and amplification, the logarithmically compressed outputs from both receivers are displayed and recorded analog on chart paper and digitally on magnetic tape. Inputs to frequency multipliers/local oscillators, timing circuits and the PRN generator are derived from another Cesium beam frequency standard.

The TOA antenna points in a fixed direction at the distant transmitter so that multipath signal components are generally at less than a 1-dB disadvantage due to the antenna elevation pattern. The AOA antenna is scanned in elevation in a continuous sawtooth pattern. The scan range extends between -0.7° and $+0.7^\circ$ with the elevation toward the transmitters on Pack Monadnock and Saddleback Mountain at $+0.1^\circ$ and -0.18° , respectively, under normal refractive conditions (earth radius factor $k = 4/3$). Antenna dynamics limit the scan speed to one 1.4° upsweep per 2.5 seconds. At this speed, pointing angle deviations from the command value can still be neglected. Actually, one sawtooth upsweep or measurement scan is conducted every 6 sec to synchronize AOA and TOA receiver operations. Experience has shown that at 15.84 GHz many of the significant temporal variations in angle-and time-of-arrival structure of atmospheric multipath signals can be tracked at this rate. Some phase-induced variations are undersampled and would perhaps be undersampled even if the scans were ten times faster. Scanning and recording functions of the AOA receiver are controlled by a microprocessor which is synchronized to the hardwired timing circuits of the TOA receiver.

The relative delay measurement between direct and multipath signal components is accomplished by stepping the receiver PRN sequence relative to the transmitter PRN sequence and determining the spacing between correlation peaks in the receiver output. With a bit length of 2.5 nsec, the width of the triangular correlation function is 5 nsec between the zero points. In order to improve delay resolution somewhat, the stepping of the receiver PRN sequence occurs in 1/4-bit increments. At one quarter bit on either side of the correlation function peak the output level drops by 2.5 dB so that 1.3 to 1.5 nsec might be considered to be the 3-dB delay resolution of this receiver. After initial turn-on or signal loss due to various reasons, the whole 1023-bit word is searched for signals. If one or more are found to surpass a selectable threshold level, then the scan range is automatically reduced to 48 bits, extending from -8 to +20 bits or from -20 to +100 nsec of the strongest signal detected during search (acquired scan). The process repeats if during the acquired scan the highest detected signal level does no longer surpass a second threshold, independently selectable from the first one.

The AOA and TOA receivers determine only the amplitude of the sum signal as a function of elevation angle and delay. Phase information, potentially available through detection of in-phase and quadrature components of the received signal, was

not obtained. The marginal short-term stability of the Cesium beam frequency standards would have significantly affected or even masked propagation induced phase changes. During a 2.5-sec sweep of the AOA receiver through its 1.4° range, a particular received signal stays within the main antenna beam for approximately 0.5 sec. Similarly, that same signal contributes to the correlation output for 0.25 sec, based on a 120-nsec delay range which is covered in 6 sec, and a width of the correlator response of 5 nsec.

According to the manufacturer's data, the maximum rms phase deviation at the Cesium standard output frequency of 5 MHz is 1.33 mrad for 0.5 sec averaging time. Multiplied by a factor of 3168, this translates into 4.22 rad at the microwave carrier frequency. The phase deviation accumulating between the multiplied output frequencies from both frequency standards is potentially higher. Over the somewhat arbitrary observation interval of 0.5 sec it may well exceed 2π , making it difficult to extract phase information superimposed by the propagation mechanism. Experimental phase observations on the TOA link during periods of undisturbed propagation appear to support the reasoning above.

The transmitter was installed inside the New Hampshire Public Television building near the top of Saddleback Mountain. The picture taken from behind the transmit antenna (the small one visible near the center of Figure 2) shows some of the foreground terrain in the Prospect Hill direction. The antenna is fed by RG-91/U waveguide.

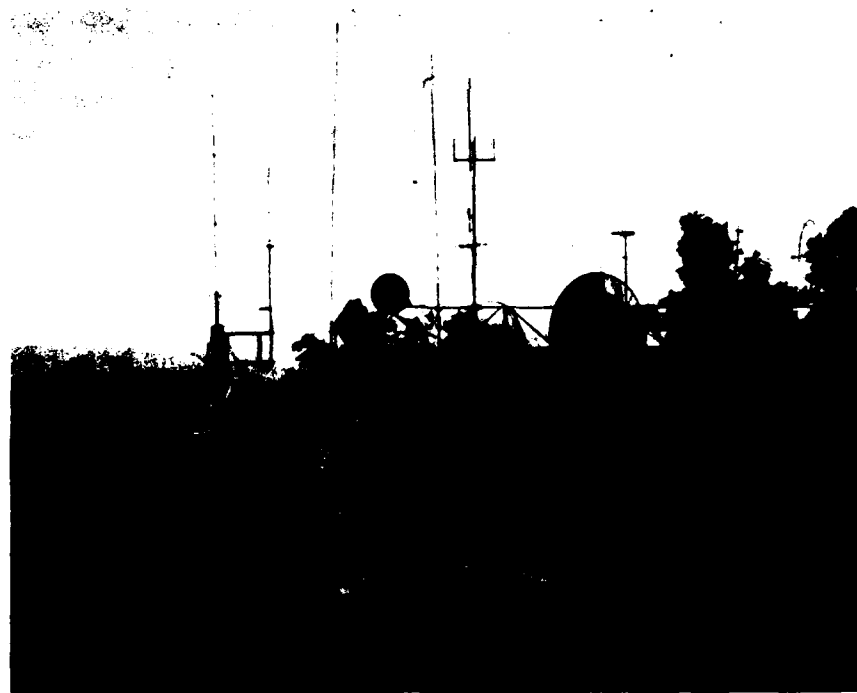


Figure 2. Transmitter Site on Saddleback Mountain

Power output from the transmitter is continuously monitored on a chart recorder. The two receiving antennas in Figure 3 are perspectively distorted in size. The 3-ft TOA dish is in the foreground, the scanning 29-ft AOA dish is in the background. The latter mounts on a concrete pedestal, 14.3 m above local terrain. The TOA antenna is attached to the laboratory building, 38.9 m to the left of the AOA antenna and 9.0 m below it when facing the transmitter. This arrangement has both advantages and disadvantages. Differences in path geometries make the AOA and TOA signals fade largely independently under atmospheric multipath conditions. This is in contrast with fading from rain attenuation when the spatial gradient in rainfall rate is not large enough to produce different effects on the two closely spaced paths. This characteristic enables one to distinguish between one and the other phenomenon. Although there may be benefits to probing with co-located apertures, our ability to interpret wave propagation mechanisms in terms of spatial refractivity structure is probably affected only to a minor degree by the separate paths.



Figure 3. AOA and TOA Receiving Antennas at Prospect Hill (29-ft Antenna is in Background)

The AOA receiver front end including the local oscillator/microwave multiplier chain is mounted on the 29-ft antenna with DC, IF, and multiplier drive signals carried by coaxial cable. The TOA receiver front end components are housed right inside the laboratory building. The antenna connects to them with RG-91/U waveguide. Figure 4 displays most of the remaining receiver, control, and recording sub-systems. Digital data recording on magnetic tape is of 12-bit resolution (AOA) and of 8-bit resolution (TOA). The AOA scan is sampled 64 times per 1.4° upsweep or once every 0.022° of antenna motion. The TOA scan is sampled 192 times per 120-nsec delay range or once every 0.625-nsec delay increment. We found experimentally that atmospherically induced delay spreads cover only a small portion of the 120-nsec range. Therefore, similar numbers of samples per scan were later processed of both AOA and TOA data. A 64-sample delay range corresponds to 40 nsec. Blocks of 64 scans constitute a record in the TOA recording format. Since the AOA scan is slaved to the TOA scan, every 64th AOA scan is suppressed, as will be seen later in samples of recordings. Much of the experimental hardware was adapted to the measurement program. This led to some peculiarities that would have been avoided, had the systems been designed from the ground up. Both systems can operate unattended over a 24-hr period, after which maintenance on the 29-ft antenna and magnetic tape change become necessary. Proper operation is remotely monitored by telephone, and the transmitter is remotely controlled by a separate radio link.

2.2 Experimental Path

The curvature of the earth makes it necessary to place transmitters and receivers at relatively high elevation if terrain obstructions are to be avoided on a long LOS path. One of the constraints imposed on our experiment is the location of the 29-ft AOA receiving antenna. It is situated on a hilltop and clear of surrounding terrain and vegetation. However, its elevation is only 159.4 m above sea level. For a pathlength approaching 100 km, the transmitter elevation has therefore to exceed that of the receiver by a substantial amount to achieve terrain clearance. As a first-order assumption, bending or ducting of microwaves in the atmosphere is due to horizontally stratified layers of increased vertical refractivity gradient. Maximum interaction requires that radio rays enter or penetrate these layers at a very shallow angle. This is negated if terrain clearance on a long path requires that one of the terminals be elevated substantially above the other. Note that such rationale is for a test link intended to be susceptible to atmospheric multipath for study purposes. Actual military communication links would be better off with large terminal height differences, a condition that sometimes cannot be achieved.

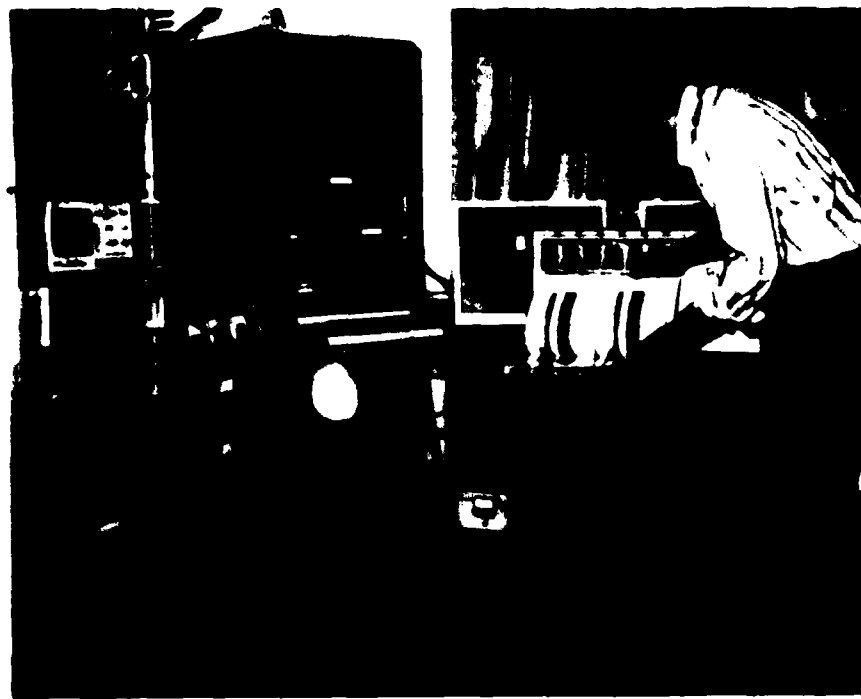


Figure 4. Receiving and Data Recording Equipment at Prospect Hill

With these restrictions in mind we found a suitable transmit site on Saddleback Mountain (pathlength 87.6 km) at 338.0 m elevation above sea level. The ratio of terminal height difference to pathlength amounts to 0.002, comparable to some of the links found in the Digital European Backbone (DEB) system. The path runs nearly north to south as seen in Figure 5 and largely parallel with the Atlantic coastline. It is too far away from the ocean for it to have a predominant influence on the propagation mechanism. The terrain is generally hilly and ascending south to north toward the White Mountains region in New Hampshire. Figure 6 shows the terrain profile. The dashed outline of Pawtuckaway Mountain close to the transmitter end of the path is several km to the east of the great circle path and not likely a source of terrain multipath. Obviously, Walnut Hill presents the greatest danger of terrain interaction.

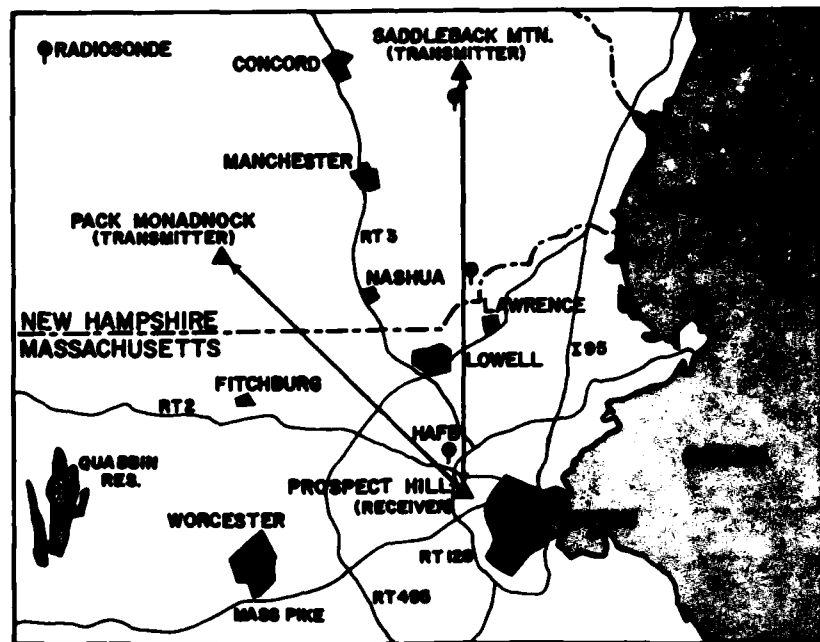


Figure 5. Saddleback Mountain to Prospect Hill Path

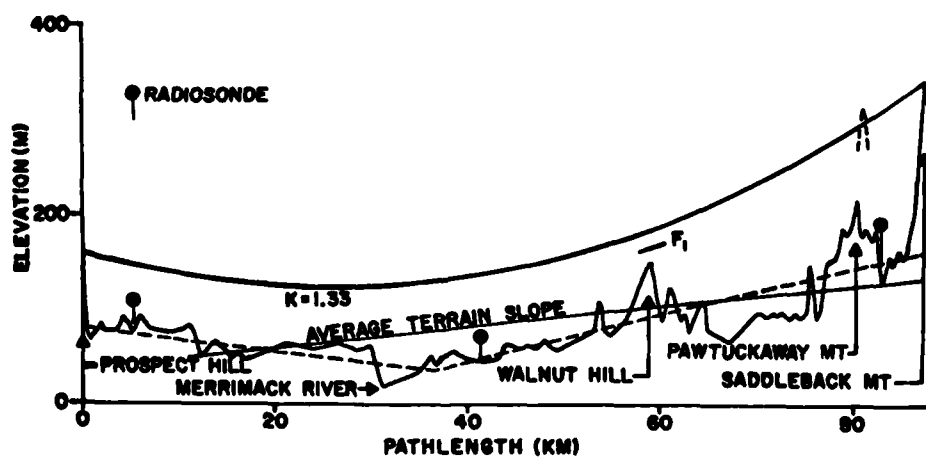


Figure 6. Saddleback Mountain to Prospect Hill Terrain Profile

This test link is not designed to meet nor does it have to meet the criteria in CCIR Report 338-4⁷ for acceptable terrain interference on communication links under subrefractive conditions. It is worthwhile, though, to investigate the potential for such interference and the ability of the measurement systems to diagnose the condition. While $k = 2/3$ is generally assumed to be the worst subrefractive case encountered anywhere, it does not prevail over long distances at the same time. Report 338-4 shows a graph according to which the minimum effective value of k increases with pathlength. Thus, $k = 0.9$ is exceeded 99.9 percent of the time on an 87.6-km path in continental temperate climate. Constructing a parabolic-arc-over-flat-earth profile⁸ as in Figure 6, one finds that the LOS ray for $k = 0.9$ passes through Walnut Hill (height 149.9 m, distance from Prospect Hill 59.5 km) at a height of 132.6 m. When $k = 1$, the ray barely clears the hill, and at $k = 4/3$ or under average refraction in the atmosphere, there is better than one Fresnel zone clearance at $f = 15.84$ GHz. There is some uncertainty in these numbers because of the limited accuracy with which the geodetic coordinates of the path terminals are known:

Saddleback Mountain	Lat.	43° 14' 34"
	Long.	71° 12' 24"
Prospect Hill	Lat.	42° 23' 18.283"
	Long.	71° 15' 15.365"

A longitudinal offset at Saddleback Mountain of $\pm 0.5''$ corresponds to an east/west shift of 11.35 m. Actually, the signal passes over the eastern slope of Walnut Hill, where the crosspath gradient is 0.87 m per 10 m. Accounting for the east/west displacement between TOA and AOA paths at the obstacle and the transmit site uncertainty, a height deviation of ± 1.5 m might accrue. Atmospheric multipath is associated with superrefractive layering. Under these conditions sufficient terrain clearance exists over Walnut Hill. Apart from the blockage problem, the level of the terrain returned signal remains of concern. With a beam-width of 1.45°, the 3-dB transmit antenna cone opens to 730 m at Walnut Hill and illuminates the terrain in this area well. Since Walnut Hill is wooded for the most part one can assume that it is a very rough scatterer at 15.84 GHz. Terrain returned components must be of considerably lower amplitude than the direct LOS signal.

7. CCIR International Radio Consultation Committee (1982) Recommendations and Reports of the CCIR, Vol. V (Prop. in Non-Ionized Media) Geneva, 1982.
8. Livingstone, D. C. (1970) The Physics of Microwave Propagation, Prentice-Hall, Englewood Cliffs, New Jersey:83.

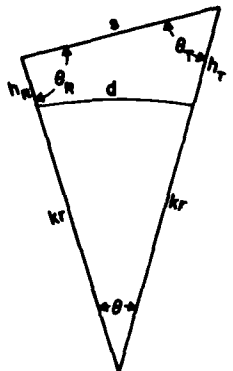
Launch angles from Saddleback Mountain and Walnut Hill and angles of arrival at Prospect Hill can be determined trigonometrically by inspection of Figure 7a. For an effective earth radius $k \cdot r$, terminal/scatter point heights h_T , h_R , LOS distance s and surface distance d , the transmit elevation angle θ_T and the receive elevation angle θ_R follow from the law of cosines

$$\theta_T = \cos^{-1} \left[\frac{s^2 + (kr + h_T)^2 - (kr + h_R)^2}{2s(kr + h_T)} \right] \quad (1)$$

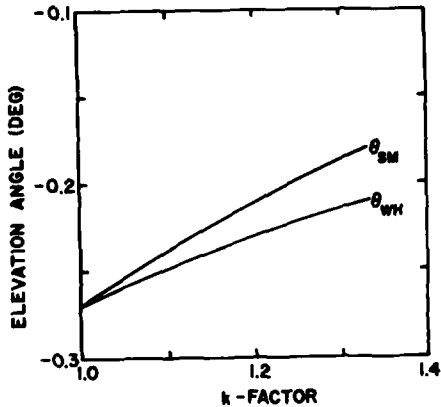
$$\theta_R = \cos^{-1} \left[\frac{s^2 + (kr + h_R)^2 - (kr + h_T)^2}{2s(kr + h_R)} \right].$$

Under normal refraction ($k = 4/3$) we find $\theta_T = -0.41^\circ$ and $\theta_R = -0.18^\circ$ (AOA antenna). It is of interest to compare θ_R -values under conditions of $k < 4/3$ to determine if the AOA antenna serves to recognize subrefractive conditions.

Figure 7b shows as a function of k -factor the elevation angles of signals arriving from Saddleback Mountain, θ_{SM} , and Walnut Hill, θ_{WH} . Under normal refraction ($k = 4/3$) the Walnut Hill signal arrives 0.03° lower than the direct signal. This is insufficient to resolve the two components with the 0.15° elevation beamwidth of the AOA antenna. The major eliminating factor against terrain returned signals must therefore be the poor scattering of the terrain. The change in θ_R versus k , however, is clearly detectable with the antenna.



(a)



(b)

Figure 7. Terrain Reflected and Direct Ray Elevation Angles vs k-Factor

The least-mean square average terrain slope was computed for the profile in Figure 6.

$$h = 39.7 + 1.1 \ell , \quad (2)$$

with h in m and ℓ in km (pathlength measuring from Prospect Hill). Layers in the atmosphere are of limited vertical extent. A ray traveling inside such a layer will change its direction more, the longer it stays within the layer. If the refractive layer is not horizontally stratified but slopes toward the line connecting transmitter and receiver, then the effective height difference between them is reduced. A constant layer height above the average terrain along our experimental path would lower the actual terminal height difference of 178.6 m by 95.9 m. Sloping of gradient layers independent of the underlying terrain is also associated with weather fronts.

2.3 Meteorological Sounding

The concept of an atmosphere with vertical refractivity gradient $dN/dh \leq -157$ N-units/km above a horizontally stratified boundary and $dN/dh = -40$ N-units/km below it, as assumed in Reference 5, serves well to explain the principle of multi-path propagation. In reality the medium is more complex in both lateral and vertical directions. For one, ducting layers are quite limited in vertical extent. Unless ducting gradients are strong, rays penetrate through the layer even at relatively shallow entrance angles, so that no multipath signal results. Layer slope and hence the lowering of relative angles between rays and layers is of substantial importance to explain observed results.^{9, 10} Also, layers frequently do not spread uniformly over the length of a long LOS path, making the actual situation more complicated than the basic model. The vertical refractivity gradient profile must be measured in multiple locations along the test path in order to aid in the interpretation of observed radio propagation phenomena.

Meteorological measurements¹¹ were made with an Airsonde, a radiosonde-type instrument. Two types of Airsondes are manufactured by Atmospheric Instrumentation Research, Inc., Boulder, CO. Both types measure the dry-bulb and wet-bulb temperatures, but the more versatile one measures the air pressure also. The Airsonde was carried aloft on a 30-gram balloon. Data from all sensors were telemetered to the ground station every 5 to 6 sec to be recorded on a cassette tape. The balloon ascent was monitored for 20 to 25 min after launch or up to the 700-mb level. On occasion the soundings were cut short when there were indications of prolonged periods of a frozen wet bulb, weak incoming signals or data rejection by

9. Barton, I. J. (1973) The importance of tilted layers in the tropospheric ducting of radio waves over the Timor Sea, Radio Sci. 8(No. 8, 9):727-732.
10. Schleher, J. S. (1982) Tilted refractive surfaces at Eglin Air Force Base, Florida, Radio Sci. 17(No. 5):1281-1284.
11. Izumi, Y., and Morrissey, J. F. (1982) Meteorological Measurements on the Monadnock-Prospect Hill Communication Link, AF Geophys. Lab. unpublished report.

the data acquisition system due to interference from other sources. In order to provide adequate resolution of the atmospheric parameters, efforts were made to control the rise rate of the balloon to between 2.0 and 2.5 m/sec. The combination of rise rate and commutation rate (data sampling rate for telemetering) results in a height resolution between 10 and 15 m. Thus the Airsonde provides much more detail than the standard radiosonde which has a resolution of about 150 m. Vertical refractivity profiles were calculated from the dry/wet bulb temperatures and pressure using standard formulas.

Since data are needed in the lower atmosphere only, tethered operation of the Airsonde appeared attractive. It makes possible continuous measurements and at least in principle very slow ascent and descent rates with correspondingly high resolution. Unfortunately, stability problems with the available balloons denied us the latter benefit, so that tethered operation was used infrequently. An acoustic prober installed at Hanscom AFB, MA near the receiving end of the path provided information on temperature inversions aloft. It served mainly as one of the criteria on which the release of Airsondes was based. Airborne measurements were made at Hanscom AFB, at Salem, NH in the vicinity of midpath and at Deerfield, NH near the transmitting end of the path. Figures 5 and 6 mark these locations. There were no permanent installations at Salem and Deerfield. Launch crews had to travel to these sites ahead of a forecast event. The radio links were powered up continuously for extended periods during the ducting season. Nocturnal and early morning ducts are likely at this time of the year during calm and clear nights when radiational cooling results in temperature inversions. The cost and labor intensive effort of probing the atmospheric refractivity structure repeatedly and at multiple locations along the test path forced us to limit this activity to days on which a high probability of ducting was forecast. In addition to cooling from below which is responsible for much of the increased duct occurrence, there are other atmospheric processes that can produce layers of enhanced temperature/humidity gradient. Subsidence and advection are examples. Weather fronts represent gradient layers with inherent tilt, not due to the tilt of the underlying terrain. Kerr¹² quotes for the slope of frontal surfaces: 1/100 to 1/300 (warm front) and 1/50 to 1/150 (cold front). However, while the temperature always increases with height, the humidity often does not, making it less likely for a duct to form along the frontal surface.

12. Kerr, D.E. (1951) Propagation of Short Radio Waves, Rad. Lab. Ser. Vol. 13, McGraw-Hill, New York:263.

Soundings were begun at the specified locations around 0600 or 0700 in the morning. Depending on the severity of the expected event, measurements were conducted at Hanscom AFB alone or at Hanscom AFB and at Salem. On very few occasions was it possible to take soundings at Deerfield as well. At times ducting did not occur at all after being forecast, or the layers formed at a height and gradient to which the radio systems were not susceptible. At other times, radio signals indicated multipath effects which were not forecast. In some of these instances, Airsondes were released at Hanscom AFB as a minimum. Based on the continued existence of abnormal radio propagation, acoustic-sounder returns and the strength and height of previously detected refractive layers, measurements were continued at approximately 1-hour intervals until mixing in the atmosphere destroyed the layers in mid or late morning.

A total of 108 refractivity profiles were obtained on 21 days between 17 August and 21 November 1983. We discuss a subset of five days during which both substantial ducting and radio interference were observed. Profiles of refractivity N and modified refractivity M vs height were plotted for each radiosonde ascent and regions of negative dM/dh or $dN/dh < -157$ N-units/km identified. Statistical information on all ducts probed during 25 August, 16, 29 and 30 September and 1 November is compiled in Table 1. Note that the data may contain probings of the same duct at several locations and times.

Table 1. Duct Parameters on Selected 1983 Days

Day	n	ΔN_{\max} N-units	ΔN_{\min} N-units	$\overline{\Delta N}$ N-units	Δh_{\max} m	Δh_{\min} m	$\overline{\Delta h}$ m	$\left(\frac{dN}{dh}\right)_{\max}$ N-units/ km	$\left(\frac{dN}{dh}\right)_{\min}$ N-units/ km
25 Aug	17	-23.8	-2.5	-11.74	89.8	11.3	50.36	-391.7	-231.8
16 Sep	21	-16.4	-2.3	-5.66	80.6	7.4	27.34	-458.2	-227.8
29 Sep	16	-22.9	-1.6	-7.63	79.6	8.1	27.20	-524.5	-261.2
30 Sep	17	-39.4	-6.5	-14.83	95.0	18.7	42.72	-740.0	-360.8
1 Nov	18	-22.4	-1.5	-5.43	102.8	7.8	26.27	-304.3	-203.9

In Table 1, n is the number of measurements which showed ducting gradients on a specific day. The values ΔN_{\max} , ΔN_{\min} , and $\overline{\Delta N}$ are the largest, smallest, and mean N -differences found between the inversion points of the M -profiles. Likewise, Δh_{\max} , Δh_{\min} , and $\overline{\Delta h}$ are the largest, smallest and mean height ranges over which ducting gradients existed. They are less than the actual duct thickness. Maximum values for ΔN and Δh do not necessarily derive from one and the same duct. This is also true for the minimum. Steepest and mean refractivity gradients

$(dN/dh)_{max}$ and (dN/dh) are listed in the last two columns. Several observations can be made in connection with Table 1. Although a duct of nearly 40 N-units strength existed at one time, on average ducts do not exceed 10 N-units. Layers with ducting gradients were found to have a thickness of up to 100 m, but more typically they range between 30 and 40 m. The maximum refractivity gradient of -740 N-units/km exceeds the mean gradient substantially. An average duct exhibits a gradient of around 250 N-units/km.

With ducts of moderate strength prevailing on the Saddleback Mountain to Prospect Hill path, their inclination relative to the transmitter/receiver line becomes of interest. In Figure 8 each of the 25 frames may be considered a replica of the path in Figure 6 with H (Hanscom AFB), S (Salem), and D (Deerfield) representing the radiosonde launch sites. Vertical bars describe the height ranges over which ducting gradients exist. The number next to them gives the total change in N-units. All five launches vertically above an "H" are made at Hanscom AFB and so on. Exact launch times are marked right with each launch if there was one at the specific time and location. The five frames in a horizontal row are hourly cross-sections of the atmosphere along the path from 0600 to 1000 in the morning. Each row represents one of the five days.

The maximum height plotted is 500 m. At a rise rate of 2 m/sec the balloon reaches this height in a little over 4 minutes. It can reasonably be assumed that the horizontal offset due to wind is negligible and that the profiles are vertical. At the bottom of the figure the black triangle gives the average terrain slope as calculated earlier, scaled to the dimensions of an individual frame. Unfortunately, of the five days shown here, measurements at all three sites were made on 16 September only, and then only in the 0700 and 0800 frames. Several parameters of the layer structure in this time interval may be implied from the frames. There were two layers in existence. In three of the cases, they are V-shaped, that is sloping down toward the center from either end of the path. The vertical spacing between the layers widens toward Saddleback Mountain from about 20 to more than 150 m. A limited amount of change occurs in the 1-hr period, except within the upper layer at midpath which goes down in height, thickness, and total ΔN . At both times the two layers are not only non-uniform in height but also in thickness and ΔN . Certainly, the non-uniformity of the underlying terrain must have to do with this. A closer inspection of the path profile in Figure 6 provides justification for a V-shaped layer profile. Two least-mean-square approximations to the terrain profile may be calculated, extending from Saddleback Mountain to the Merrimack River to Prospect Hill. The straight-line sections

$$h = 81.9 - 1.16 l \text{ and } h = 50.3 + 2.46 l, \quad (3)$$

with h in m and l in km are plotted in Figure 6 as dashed lines. The intersection of the two lines at the low point of the two-segment profile is within 5 km of the center sounding location. With no Deerfield data in all other frames except for the earliest one on 16 September, it cannot be ascertained that the V-shaped layer structure is typical along the path. Qualitatively, a down slope from Prospect Hill toward Salem is seen in many frames. This is not always the case, however. Note that mostly two or three layers existed at one time. Different numbers of layers identified at different locations at approximately the same time make it difficult to associate the soundings with one another.

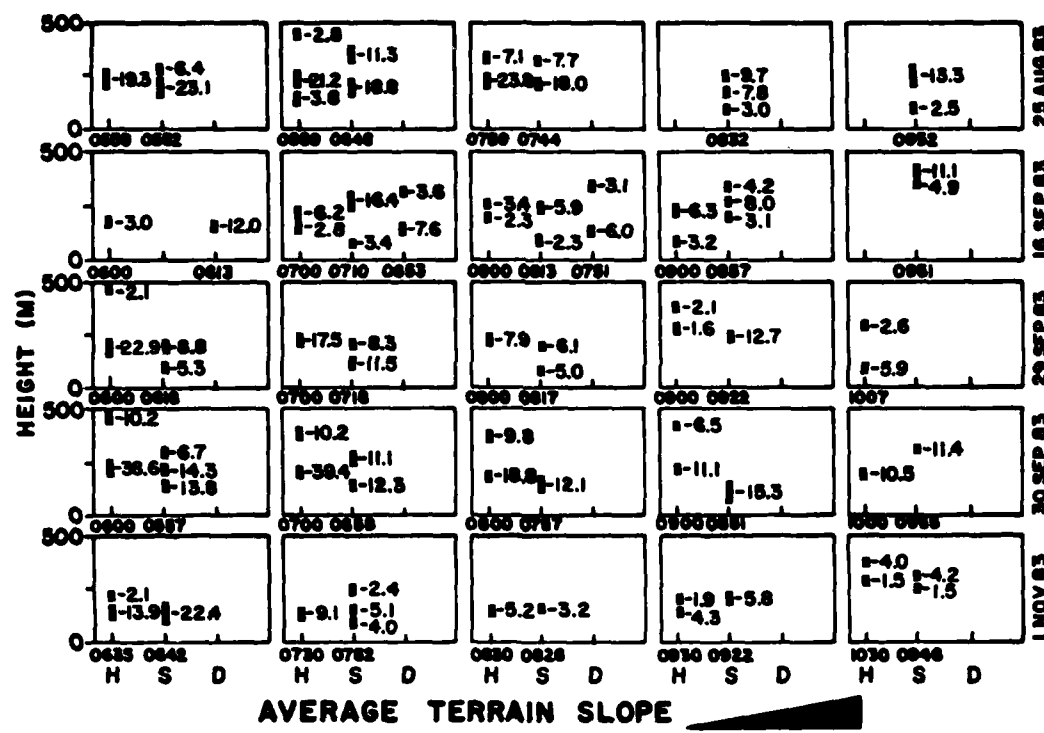


Figure 8. Height Regions With Ducting Gradients vs Launch Positions Along Path and Launch Times

The total change in N-units across layers shows about the same degree of variability with location and time as the associated heights do. Figure 8 suggests that the layer structure in the atmosphere over our path is quite complex and time variable, even with the limited number of soundings obtained. More closely spaced

sampling in time and location would probably reveal an even greater complexity. This must be borne in mind when modeling the wave propagation mechanism or interpreting the observed radio signal in terms of measured refractivity profiles.

3. PROPAGATION ANALYSIS

Depending on the particular objective, several approaches are possible in modeling atmospheric LOS multipath. Rummel¹³, being interested in the statistical properties of the fading signal, treats the atmosphere as a "black box" and finds that multipath can be adequately described by three-phasor interaction. The parameters are chosen for a best match to observed data, but have no strong connection to the physics of wave propagation. Pickering and DeRosa,¹⁴ on the other hand, model LOS multipath propagation in a physical sense, if greatly simplified by assuming the upper and lower halfspace geometry previously mentioned with constant refractivity gradients in both regions. Under this condition and for ray paths shallow relative to the boundary between the halfspaces, ray paths can be approximated by circular arcs. The number of possible multipath rays, their arrival angles and relative differences in delay are then linked to the path geometry and refractivity gradients by a quartic equation. Parl⁵ uses the same atmospheric composition and derives solutions of the quartic equation valid for all transmitters and receiver heights relative to the layer interface. He shows that multipath rays appear in groups, increasing in numbers as the refractivity gradient in the upper layer becomes more negative and the terminal heights approach each other. The number of rays is always odd and equal to $3 + 4p$ where p , the order of rays, is an integer equal to or greater than zero. For the maximum number of multipath rays to exist under given conditions of refractivity gradient and terminal height difference, the interface has to be located at a specific height. In a qualitative way, zero-order multipath rays are shown in Figure 9. Three situations are distinguished: (a) both transmitter and receiver are in the ducting layer, (b) one terminal is in the ducting layer, the other in the nonconducting layer, and (c) both terminals are in the nonconducting layer. Depending on the particular ray, m crossings of the interface occur, with $m = 0, 1, \text{ or } 2$. The circular rays penetrate the boundary without a discontinuity in slope. Differences in path delay derive from the differences in pathlengths and propagation velocity. The takeoff and arrival angles in Figure 9 are exaggerated.

13. Rummel, W. D. (1979) A new selective fading model: application to propagation data, Bell Syst. Tech. J., 58(No. 15):1037-1071.
14. Pickering, L. W., and DeRosa, J. K. (1979) Refractive multipath model for line-of-sight microwave relay links, IEEE Trans. on Comm. COM-27(No. 8):1174-1182.

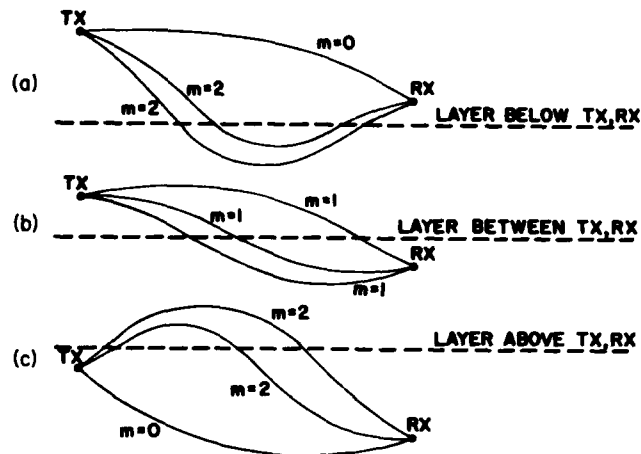


Figure 9. Three-Ray Multipath vs Layer Height

3.1 Model Calculation

Using the formulation and computer program of Parl and Malaga² we have calculated AOA and TOA data for the Saddleback Mountain to Prospect Hill path. In Figure 10 elevation angles of component rays are plotted vs the height difference between the layer interface and the receiver. The pathlength is $d = 87.6$ km. We assume a terminal height difference of 100 m. Since the actual sea level height difference between terminals is 178.6 m, this implies the layer interface slopes down 78.6 m from transmitter to receiver. Refractivity gradients of -300 N-units/km in the upper and -40 N-units/km in the lower halfspace result in a maximum of three multipath rays when the layer interface is within a specific height range. Negative layer heights in Figure 10 represent the case in Figure 9a. Note, however, that under the conditions chosen in Figure 10 no multipath propagation of the type shown in Figure 9a exists. Refractivity gradients or terminal height differences would have to be adjusted. With the layer boundary between receiver and transmitter heights (Figure 9b), Figure 10 predicts up to three multipath rays. As the boundary moves up to the transmitter height and beyond, again Figure 10 indicates no multipath propagation. Multipath components as seen in Figure 9c result from more extreme parameters.

In an atmosphere of normal lapse rate (-40 N-units/km) the single LOS ray arrives at -0.22° . It rises to 0.43° if the lapse rate is -300 N-units/km. These angles are measured relative to the interface slope and are 0.05° more positive for a 178.6 m terminal height separation. Under the selected conditions multipath propagation occurs with the layer boundary 37.25 to 81.85 m above the receiver. The largest possible difference in elevation angle between multipath components is 0.52° .

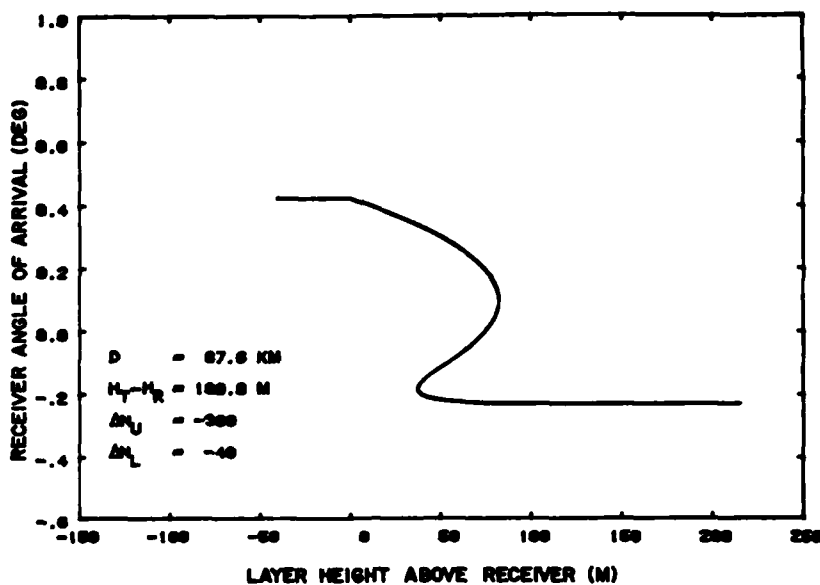


Figure 10. Computed Multipath Angles of Arrival

A corresponding plot of relative path delay is shown in Figure 11. Only relative delays between multipath rays are of interest. The delay axis is labeled in nanoseconds of delay relative to the delay of a fictitious ray traveling along the layer interface between the perpendicular projection points of transmitter and receiver onto the interface. As the layer height reaches 37.25 m and multiple rays are supported by the medium, a maximum delay spread of 1.3 nsec results. The ray with the highest elevation angle is the fastest to reach the receiver. It travels at greater height than the other rays and hence through a region of lower N and at greater speed. With increasing height of the layer interface, the delay spread decreases until the originally fastest ray is overtaken by one of the new multipath rays. The delay spread then increases again up to an interface height of 81.85 m above the receiver, where approximately 1.3 nsec is reached again before the original ray and one of the new multipath rays vanish. It is apparent from Figures 10 and 11 that the two new multipath components should be more easily detectable by their angular separation than by their delay separation, as the layer interface passes through the critical height.

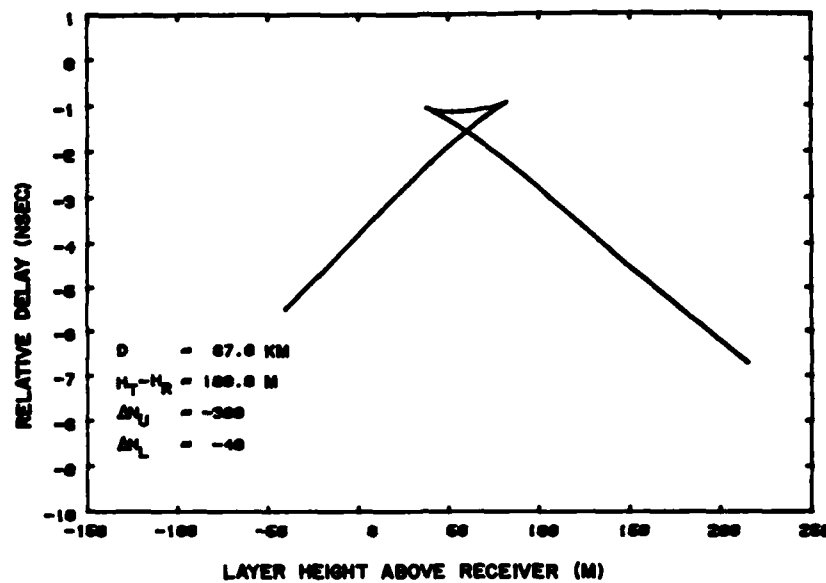


Figure 11. Computed Multipath Delays

Figure 12 provides further insight into the propagation mechanism. The height of each component ray above the layer interface is plotted vs the latter's height above the receiver. Although the model assumes an infinite thickness of the ducting layer, this figure yields minimum layer thicknesses, for which multipath propagation would occur as if the layer were of infinite thickness. Thus, with the ducting layer positioned 37.25 m above the receiver, it must be at least 153 m thick to support all three multipath rays, and at least 66 m thick to support the lower two rays. This minimum required layer thickness changes with layer height above the receiver. Assuming that the layer height is chosen optimally, that is, it is placed such that a minimum thickness is required to support two or three multipath rays, the dependence of this minimum layer thickness on the refractivity gradient inside the layer and the height difference between transmitter and receiver is shown in Figure 13. The points are taken from Figure 12 and similar plots with appropriately selected parameters. Obviously, a greater layer thickness is required to propagate three multipath rays than to propagate two. This is true for all gradients and at least to the actual terminal height difference of 178.6 m. At $dN/dh = -200 \text{ N-units/km}$ there is only a single ray at 178.6-m height difference. No point is shown. Depending on the terminal height difference, the layer must be between 46.3 and 119.1 m thick in order to sustain three rays. If one of the three rays is permitted to escape through the top of the duct, then a thinner layer will still permit two rays to reach the receiver. The corresponding range of thicknesses is

27.2 to 81.7 m. The curves for two-ray and three-ray multipath propagation are closest to each other at -200 N-units/km and furthest apart at -500 N-units/km. Given the limited ΔN of actual layers, this appears to suggest that the likelihood of three rays decreases with increasing refractivity gradient. At a 100-m effective height difference between terminals and a gradient of -200 N-units/km three rays require a layer of 74.6-m thickness or $\Delta N = -14.9$ N-units. At the same height difference and -500 N-units/km gradient two rays are supported by a 35.2-m layer of $\Delta N = -17.8$ N-units. These numbers are possible according to Table 1. Values as high as $\Delta N = -39.4$ N-units were measured on the five days reported, although $\Delta N = -10$ N-units is more typical. The conclusion must be drawn that three-ray multipath interaction on the Saddleback Mountain to Prospect Hill link is most likely based on sloping layers of relatively great thickness and moderate refractivity gradient. Such conditions are met infrequently.

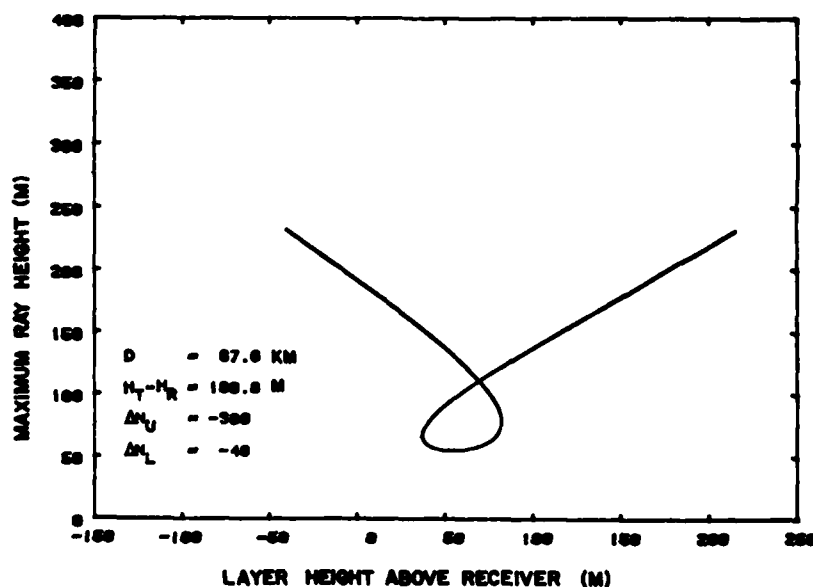


Figure 12. Computed Ray Penetration Depth Into Ducting Layer

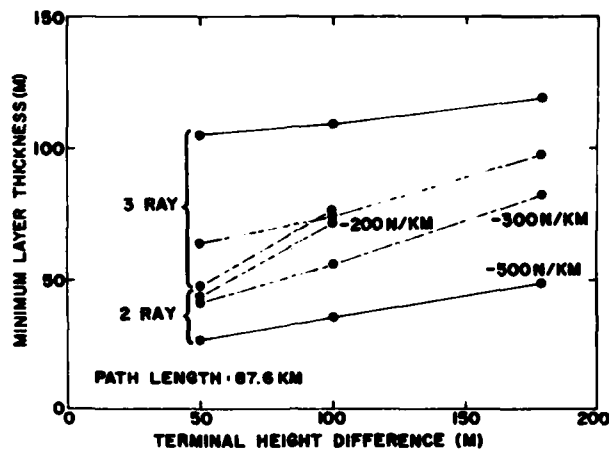


Figure 13. Minimum Layer Depth for Multipath Propagation

Since rays propagate on circular paths in a constant-gradient medium, it is simple to find the lengths of their travel in such a medium, given the depths to which they penetrate it. Results from Eq. (4)

$$s = \sqrt{h(2 \cdot 10^6 / (dN/dh) - h)} \quad (4)$$

are plotted in Figure 14. To continue with the case of three-component multipath in a 74.6-m thick layer of $dN/dh = -200$ N-units/km, this layer must extend for a minimum of 55 km along the transmitter to receiver direction. In other words, the layer must cover nearly the entire pathlength. If we consider a two-component multipath situation within a 35.2-m thick layer of $dN/dh = -500$ N-units/km, then the layer must cover a specific portion along the propagation path, at least 24 km in length. This serves to illustrate the spatial extent of gradient regions in the atmosphere, necessary to bring about line-of-sight multipath propagation. The assumption of horizontal homogeneity in the medium, implicit in the term "refractive layer" and basic to the modeling of Parl⁵ and others, is not a condition required for multipath propagation. Ray tracing through height and pathlength dependent refractivity structures shows this. The model calculations, however, give an indication of the equivalent size of refractive gradient structures necessary to produce multipath. The examples suggest that sampling an 87.6-km path in three locations should reveal this equivalent structure in many instances.

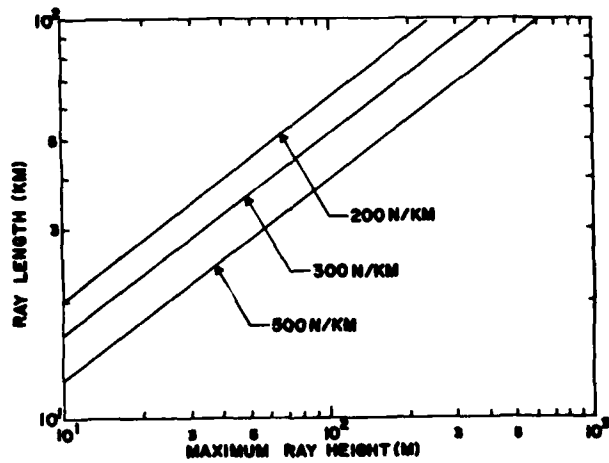


Figure 14. Length of Ray Path in Ducting Layer

3.2 Scan Simulation

To aid in the interpretation of observed elevation angle and time delay scan patterns under multipath propagation conditions, the AOA and TOA receiver output is simulated. We assume up to three multipath rays of amplitude A_j , phase angle ϕ_j , respectively delay τ_j , and elevation angle β_j . The elevation beam pattern of the scanning antenna is approximated by an exponential function. The delay response is represented by a triangular function. That is, when the binary code of a received multipath component is exactly synchronized with the reference code generated in the receiver, the output is at its maximum. The output is zero when the received multipath code is advanced or delayed by one bit or more. For misalignments of less than one bit, the receiver output varies linearly between its maximum and zero.

Figure 15 shows the AOA scan procedure. Rays 1, 2, and 3 arrive from different directions at the receiving antenna. One of the cases of Figure 9 serves to demonstrate this. The main beam plus two upper and two lower sidelobes scan through the set of rays with the main beam center line traversing the angular range from minimum to maximum elevation. The sidelobes are included because of the logarithmic receiver response. Lower-level signal variations observed in actual multipath scans are the result of either main beam or sidelobe activity. The voltage gain of the main beam or a sidelobe can be written as

$$G_i = G_o \sqrt{\exp(c(|\beta - \beta_0|)^n)} \quad (5)$$

with

- G_o gain factor,
- c beamwidth factor,
- β main beam elevation angle,
- β_o angular offset from main beam.

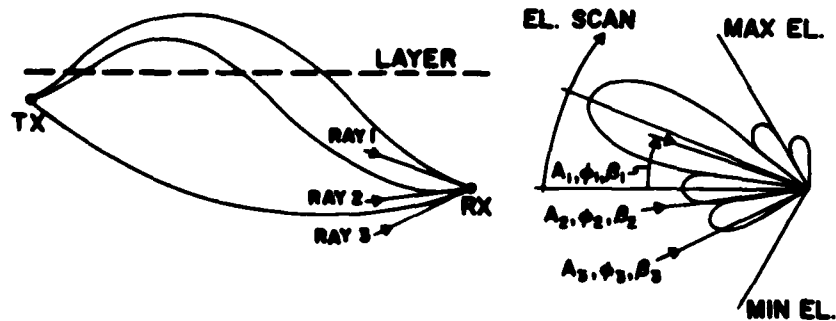


Figure 15. Simulated Angle-of-Arrival Scan

The values in Table 2 were selected for a best fit to the measured elevation pattern of the 29-ft antenna. Sidelobe gains relate to the main beam gain which is set at 1.

Table 2. Parameters Used in Elevation Beam Model

Lobe	G_o	$c (\text{deg}^{-n})$	$\beta_o (\text{deg})$	n
Second upper sidelobe	0.0479	-432	0.36	2
First upper sidelobe	-0.123	-432	0.22	2
Main lobe	1	-488	0	2.5
First lower sidelobe	-0.0661	-432	-0.22	2
Second lower sidelobe	0.0389	-432	-0.36	2

With the composite antenna pattern pointing in a specific direction, its response to three rays arriving from different angles of elevation is computed in the following manner. The gain of each lobe in the direction of one of the multipath rays is determined. The voltage gains of all lobes

$$G = \sum_{i=1}^5 G_i \quad (6)$$

are summed. The first upper and lower sidelobes are negative because of phase reversal. Real and imaginary components of this ray ($j = 1$)

$$R_j = A_j \cos \phi_j \quad I_j = A_j \sin \phi_j \quad (7)$$

are multiplied individually by G to obtain their contributions to the sum signal. For the same antenna pointing angle, the real and imaginary components of the other two rays ($j = 2$ and $j = 3$) are determined in the same manner and added to the real and imaginary components of the first ray as appropriate. The magnitude of the phasor sum M , plotted in subsequent figures as a function of antenna elevation angle, is then derived from

$$M = 10 \log \left[\left(\sum_{j=1}^3 R_j \right)^2 + \left(\sum_{j=1}^3 I_j \right)^2 \right]. \quad (8)$$

Figure 16 illustrates the summation process of multiple rays received by the TOA system. Because of the logarithmic receiver response, two sidelobes in the delay domain comparable in amplitude to those of the AOA antenna were observed experimentally. For a better comparison with measured data they have also been included in the simulation. As the TOA receiver scans through its delay range, the magnitude of the sum signal is determined in a form similar to the one outlined for the AOA receiver. The voltage gain of the correlator response or its sidelobes can be written as

$$G_i = G_o (1 - |\tau_i - \tau - \tau_o| / \Delta\tau) \text{ for } |\tau_i - \tau - \tau_o| \leq \Delta\tau \quad (9)$$

$$G_i = 0 \quad \text{for } |\tau_i - \tau - \tau_o| > \Delta\tau$$

where

G_o gain factor,
 $\Delta\tau$ width of correlation function (2 bit),
 τ_o delay offset from main lobe,
 τ main lobe delay.

The parameters in Table 3 were selected to best match the experimentally observed correlator output pattern.

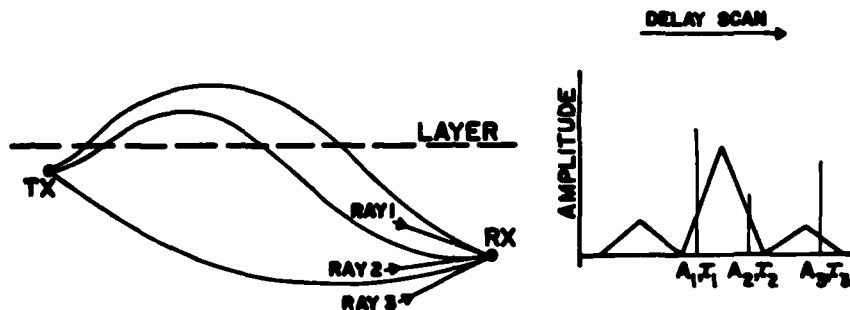


Figure 16. Simulated Time-of-Arrival Scan

Table 3. Parameters Used in Correlator Model

Lobe	G_o	$\Delta\tau$ (nsec)	τ_o (nsec)
Leading Sidelobe	0.0562	5	5
Main Lobe	1	5	0
Trailing Sidelobe	0.0562	5	-5

As before, the gain of each lobe at the delay of one of the multipath rays is determined. The sum of the gains

$$G = \sum_{j=1}^3 G_j \quad (10)$$

is formed. Real and imaginary components are multiplied with G and the magnitude of the sum vector is derived as in Eqs. (7) and (8). Plots in subsequent figures are of M vs scan delay.

3.3 Test Case

It is of interest to study the results of simulated elevation angle and delay scans through a multipath scenario of known parameters. For this purpose we have chosen the model case of Figures 10, 11, and 12. We assume that the lower boundary of the ducting layer rises from a height below that where multipath propagation appears to a height above that where multipath propagation ceases. The thickness of the layer must be sufficient according to Figure 12 to support all possible multipath rays as the layer rises. From Figure 10 we know that multipath conditions exist when the lower boundary is between 37.25 m and 81.85 m above the receiving antenna. This requires that the layer slopes upward toward the transmitting antenna for an

effective height difference of 100 m between terminals as stated earlier. We select a range for the location of the lower boundary of the ducting gradient layer between 30.31 m and 88.79 m. Simulated elevation angle and delay scans using parameters of the experimental hardware are performed at 119 equi-spaced positions within the 58.48-m height range. That is, a scan differs from the next one by a layer height change of approximately 0.5 m. One scan each occurs at the exact locations where the three multipath rays start out as two before the dual ray splits up and again where they merge into two before the dual ray disappears. A total of 119 sets of amplitude, elevation angle, and delay data, each for one, two, or three rays as appropriate were put into the simulation routines. Elevation angle and delay data are the same as those plotted in Figures 10 and 11. Parl⁵ calculates multipath amplitudes from ray density. It is well known that this procedure breaks down near caustics. We estimate approximate amplitudes from Parl's results, assuming values 10 dB higher at the caustic than under free-space conditions.

The simulated responses of our experimental AOA measurement system to the multipath structure, changing as the gradient layer rises, is seen in Figure 17a. The lowest layer height corresponds to the bottom trace in the figure. Traces are densely stacked in the vertical direction for a better visual perception of continuities in the development of multipath patterns. The dense stacking leads to some overlap between curves, since the simulation program does not eliminate hidden lines. Every fourteenth scan has been extracted from the complete sequence and replotted in Figure 17b for closer inspection. The coordinate system at the bottom of the figure indicates amplitude and angular scales. The leftmost point of each scan is at the origin of its individual coordinate system. All amplitudes are on a relative scale with 0 dB that of the received signal under no-multipath conditions.

During the first 15 scans a single wavefront arrives close to the upper end of the scan range. The signals received by sidelobes and main lobe are clearly distinguished. As the layer rises, the arrival angle is lowered. This is the consequence of a larger and larger percentage of the wave's travel taking place in the non-ducting medium. With reduced ray curvature both launch and arrival angle must be lower for a wave to reach the receiving antenna. During the final 14 scans, when again only one propagation path exists, the angle of arrival is lower by about 0.5°. The major feature of Figure 10, the question mark shaped distribution of arrival angles is well recognizable in Figure 17, if inverted due to the choice of axes. The sudden appearance of two multipath components of +10 dB amplitude each and of equal phase during the 15th scan (and their disappearance after the 105th scan) are a shortcoming of the model. Abrupt onset or loss of signal components like this were not observed experimentally.

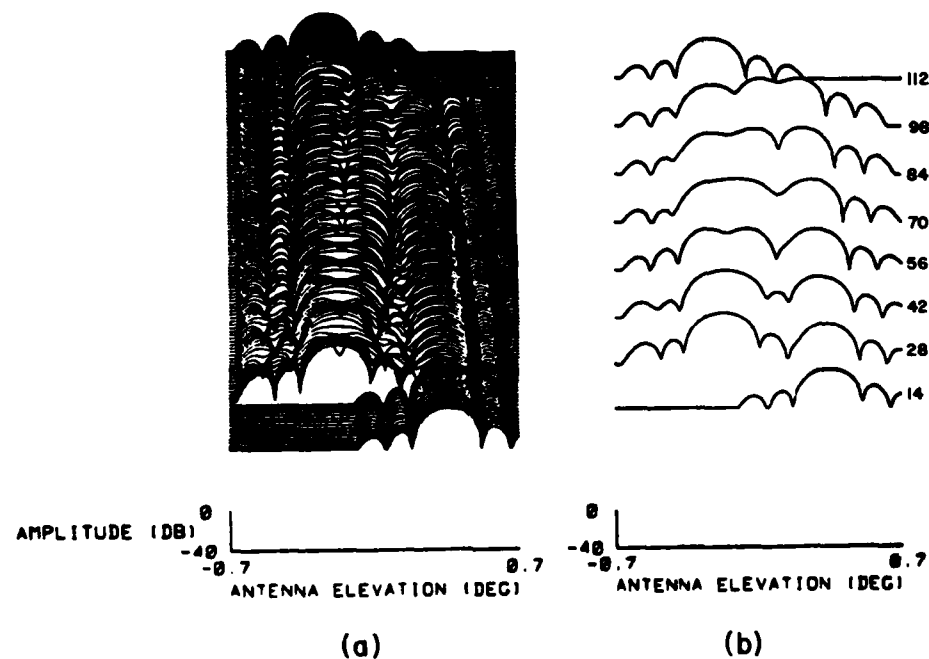


Figure 17. Simulation of Multipath Structure Due to Rising Ducting Layer as Resolved by AOA System

The upper signal is well separated in angle of arrival from the lower pair when they originate. There is interaction between sidelobes from this point on. Some slight scalloping occurs on the upper signal as well as periodic broadening. This is due to the lower two signals entering through the lower sidelobes when the antenna points in the direction of the upper signal. The phase relationship between the component signals follows from the curve in Figure 11. Although the maximum delay difference in this figure is only 1.3 nsec, it corresponds to a phase difference of 129.4 rad at the carrier frequency of 15.84 GHz. Relative delays between pairs of rays change between this maximum and zero. Hence, multiple complete phase revolutions occur between component signals as the layer rises. Figure 17 shows the effect of extensive phase change in many ways. It is obvious that the number of scans plotted is necessary mainly because of this phenomenon.

The beginning separation of the two lower multipath components from the 15th scan on is a good demonstration of phasing effects, while the antenna is essentially unable to resolve the two components in elevation angle. Both lower signals are in phase with each other when they appear. After the 22nd scan, the in-phase condition has essentially changed to an out-of-phase condition with a notch showing up in the center of the pattern and the overall width increasing. This must not be confused with the genuine double-peak resolution such as between the dual lower peak and

upper peak in scan 15. The notch between the separating two lower rays is largely due to the phase condition. The phasing notch in scan 22 is not likely the point of greatest cancellation in this area. Scan location and phasing are not coordinated. As a matter of fact, close inspection of subsequent scans reveals that a more perfect out-of-phase condition can be observed on occasion. With the 27th scan the lower two components are in phase again and the sum pattern width is narrower. This process repeats as the lower two signals move away from each other in elevation angle. Slowly, genuine angle resolution takes over from phase-derived "resolution". The latter must not be discounted, however, since it yields distinctly the existence of the two components during their early phase of separation. On the other hand, with appropriate phasing some traces in the mid to upper range of Figure 17a are seen to show hardly any undulation at all in the center portion. The left cusp of Figure 11 indicates that the delay difference between the two rays increases with layer height at a greater than linear rate. This is also seen in Figure 17, where the spacing of phasing notches increases with scan number. In contrast with the slow phasing between the lower two components in the 15th and subsequent scans, their combined phasing with the upper ray occurs at a substantially higher rate. This is quite evident by the rate at which the left side of the upper main lobe response narrows and widens. Figure 11 confirms it. The difference in slope between the two branches of the left cusp is much less than between that of either one and the third branch associated with the upper ray.

Similar observations can be made with regard to the merging center and upper rays. The two main beam responses are well separated at the 15th scan. The closer they approach each other, the more influential becomes their mutual phase relationship. Because of the model assumptions for component amplitudes, the upper ray pair disappears with the 105th scan. During this scan the upper two components reach +10-dB amplitude. Except for the abrupt onset and loss of the ray pair at full amplitude, amplitude effects do not seem to distract from the main features of the simulated scan sequence.

Sidelobe signals, to the extent that they are not masked by the main lobe responses, show interesting developments of their own. The leftmost (upper) sidelobe response to the lowest ray in Figure 10 does not change its angular location within the 1.4° scan range much over the whole sequence of scans. The rightmost (lower) sidelobe response to the upper ray in Figure 10 appears at decreasing elevation as the layer rises. This is in agreement with Figure 10. The interference to the leftmost sidelobe signal disappears at a rate almost inconsistent with the rate at which the dual main lobe signals move away from each other. In contrast, the next sidelobe signal (from the first lower sidelobe) shows phasing effects for as long as the center ray is in existence. Note how the first several maxima of the two leftmost signals can be imagined to belong to diagonal "ridges" running from the

lower left to upper right of the display. This phenomenon was observed quite strikingly on several experimental AOA scan sequences. Compare Figure 21 around 0920. Although the appearance of a ray rapidly rising in elevation angle exists, this is not likely the case. The sidelobes on the opposite side of the dual lower main lobes seem to have the character of ridges moving from the lower right to upper left.

The corresponding simulated scan sequence for the TOA receiver is displayed in Figure 18. In keeping with the experimental data collection, the vertical axis represents the logarithm of the amplitude. Again, the complete sequence of 119 scans is plotted on the left side (Figure 18a) and every 14th scan is extracted on the right side, (Figure 18b). In contrast with the AOA case, where the antenna beam clearly resolved the two major lobes at the onset of multipath, this is not so with the TOA case. The delay difference of 1.3 nsec arising with the 15th scan keeps the main lobe as well as the sidelobe responses overlapped. This continues during the whole multipath interval. The onset and disappearance of multipath rays is clearly distinguishable as such. However, this results partly from the abruptness with which the modeled rays come into existence and from the sharp delineation of the sidelobes, as they rise through the -40 dB detection level. Experimentally, the sudden amplitude changes do not occur. Besides, a noisy signal of lower level continues beyond the first sidelobes. This variable, and potentially terrain-induced signal masks subtle developments such as seen in Figure 18a at the outer edges of the sidelobes. The boundaries follow the three branches in Figure 11.

Because of the close spacing in delay between the three signal components (in terms of the system resolution), multipath effects in Figure 18 take largely the form of phasing patterns. One difference between AOA and TOA scans in the last two figures is quite apparent. The periodicity due to phasing, seen in many different ways in the AOA scans, is much harder to discern in the TOA scans. The reason is that the TOA case is in effect below the system's resolution. The signal component with the greatest offset in delay (the one existing before the other two appear when the layer rises) possesses both a rapid rate of phase change relative to the other two and an amplitude not significantly decreased by the correlator gain. This condition is essentially maintained throughout the scan sequence. That is, all signal components are, at most, moderately affected by the correlator gain function and at least one component phase changes rapidly with respect to the others. The phase relationships are identical in the AOA and TOA cases. However, it is the concurrent reduction in gain on the component with the most rapid phase change which makes the AOA display look more well behaved. We tested this assumption by deleting the original single ray artificially. The resulting TOA sum pattern from the remaining two components shows well developed periodicities as outlined for the AOA case.

Conversely, the sidelobe structure in the center region of Figure 17 has some similarly random looking variations as Figure 18. We assume that comparable contributions from all three components are the cause.

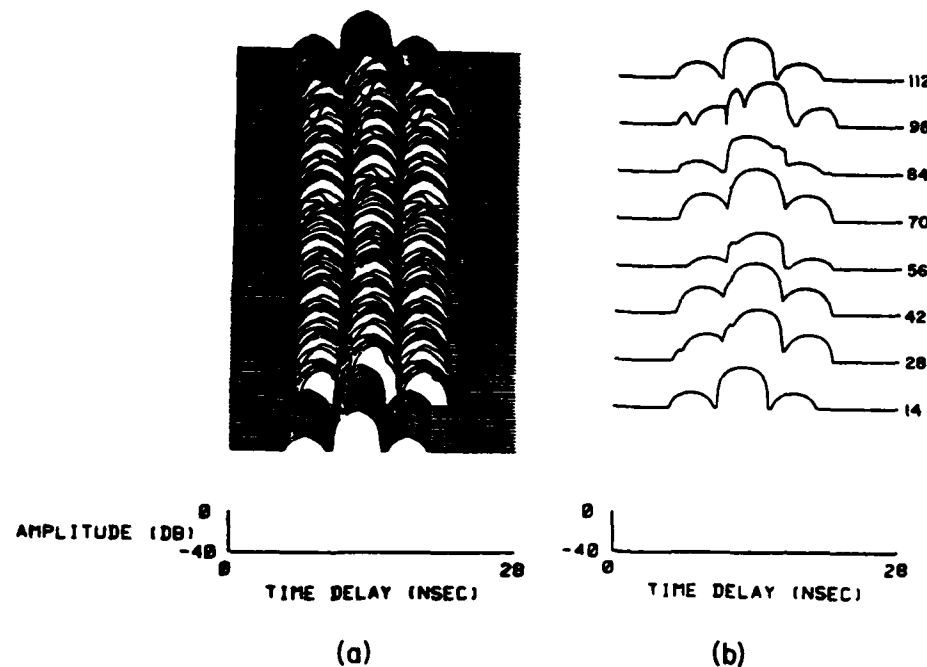


Figure 18. Simulation of Multipath Structure Due to Rising Ducting Layer as Resolved by TOA System

Inspecting now the individual scans in Figure 18b we find the ragged appearance of the whole sequence confirmed in individual traces. The second one from the top, scan 98, is most severely disturbed. In this particular case the component signals have amplitudes and delays of $A_1 = 2.458$, $\tau_1 = -1.044$ nsec, $A_2 = 2.353$, $\tau_2 = -1.004$ nsec, $A_3 = 1$, $\tau_3 = -2.097$ nsec. The delays translate into phase angles of $\phi_1 = -193.3^\circ$, $\phi_2 = 325.2^\circ$, and $\phi_3 = -77.9^\circ$. Since amplitudes A_1 and A_2 are nearly equal, their vector sum is in almost perfect phase opposition to the third vector. The amplitude ratio between vector sum and third vector is approximately equal to 2. Under such conditions the difference between the vector sum and the third vector, multiplied by correlator gain functions spaced about 1 nsec apart, leads to the pattern shown in Figure 18b. Sidelobe and main lobe responses vary independently of each other. This is confirmed by several others of the spaced scans. The first and last scans are single-signal scans and serve for reference. Logically,

sub-resolution effects on the measured TOA data require greater attention than those on the measured AOA data. In the following section we address the implications of two-signal interaction within the delay resolution cell in a systematic way.

3.4 Sub-Resolution Effects

A construct to help visualize the interaction between two component signals in a simplified and idealized fashion is shown in Figure 19. Note that the amplitude scale is linear for easier reference and that the sidelobes have been dropped. Figure 19a depicts two-ray interaction for nine delay increments τ , where τ was chosen as 1/4 bit width. Between coincidence and complete separation of the two correlator responses lie 2 bits or 8 delay steps. The light trace of amplitude 1 represents the reference and the light trace of amplitude 1/2 the delayed signal. The amplitude ratio is arbitrary. The heavy solid trace represents the resultant waveform if both components add in phase. This type of waveform is observed only when the propagation path difference between components amounts to an integral number of wavelengths or the phase difference between the RF carriers is 0° . The dashed trace represents the opposite extreme. The path difference equals a multiple of half the wavelength. The phase difference is 180° and the components subtract within the overlap interval.

Figure 19b shows the stacking of the same sequence in three-dimensional form. It is done separately in order not to clutter the subsequent figure. Only the thin-lined components are drawn. In Figure 19c the individual components are relegated to their envelopes and form two intersecting prisms. The maximum and minimum resultants are also shown at scans of 0, 4 τ , and 8 τ delay. The "damped" sinusoid that oscillates between the heavy solid and dashed lines from 0 to 4 τ marks the actual amplitude observable at the peak of the reference signal. In the example case only four RF cycles were assumed per bit width. In the TOA system there are 39.6 cycles (15.84 GHz \times 2.5 nsec) over the same interval. Obviously, the ratio of path difference and wavelength can be any non-integer. For a demonstration we have selected in Figure 19d the case of $15/6 \tau$ which corresponds to a phase angle difference of $\phi = 300^\circ$. The circled dots in (c) and (d) are identical. The sum signal, dotted in the latter figure, is a result of the assumed amplitudes, the delay difference, and the phase difference. The dotted curve falls in between the heavy solid and dashed curves as expected.

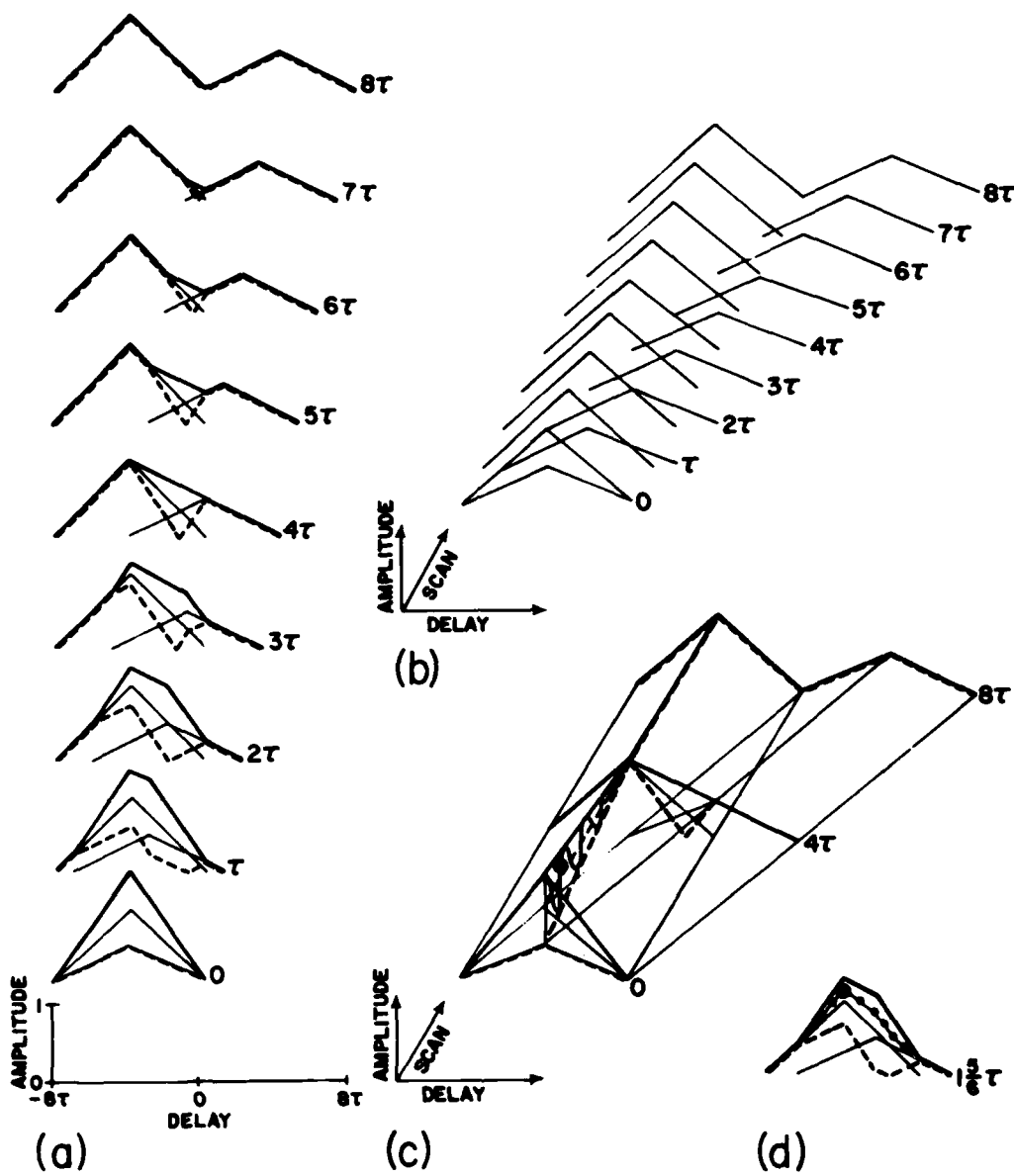


Figure 19. TOA Two-Signal Sub-Resolution Interaction; — Component Signals, - Sum Signal, ($\Delta\phi = 0^\circ$), - - Difference Signal ($\Delta\phi = 180^\circ$). (a) Delay step $\tau = 1/4$ bit per scan, (b) 3-D scan sequence (components only), (c) 3-D scan envelopes and sum signal peak vs RF-phase (damped sinusoid), and (d) Sum signal for $\Delta\phi = 300^\circ$ (circled dot identical in (c) and (d))

Several general observations can be made from Figure 19. Direct measurements of amplitude and delay are possible, when both components are separated by two or more bit times. As delay differences decrease from two to one bit time, phasing in the overlap area makes it progressively more difficult to resolve component parameters. Within this delay range the peak of the delayed component is still discernible regardless of phase. An argument might be made that with an apparent multipath peak at a delay greater than one bit time, component amplitudes and delays are measured correctly (see Figure 19a, scans at 5τ , 6τ , and 7τ).

As delays decrease from one toward zero bit times, separate and distinct peaks occur in the sum pattern that do not relate to the amplitudes and spacing of the components in a very obvious way. This can be most easily seen in the dashed traces of scans τ , 2τ , and 3τ . In these instances of 180° phase difference, the separation between apparent peaks is 1 bit although the actual delay between the components is under 1 bit. For other phase angles in this regime apparent peaks will be less discernible, depending on the particular phase and amplitudes involved. Apparent delays may be less than 1 bit, but will not generally represent the true delay difference between components. Also, the uncertainty associated with amplitude measurements increases as the delay difference approaches zero.

It is interesting that a 90° phase relationship produces a resultant equal in amplitude to the higher of the two components at all locations within the scan. Experimental scan sequences based on our system parameters and the changes in the propagation medium are likely to show two-phasor interactions with slowly varying amplitudes and delay yet rapidly changing phase. The comparison between traces of essentially constant parameters except for phase provides additional diagnostic capability.

The breakpoints in the composite curves in Figure 19a indicate the beginning, peak, or ending of a component curve. In addition, a breakpoint may result at the crossover point. If the components are exactly out of phase, the sum signal goes to zero. For any other phase relationship there is a local minimum. No break is seen under in-phase conditions. The sum waveform segments are straight lines. The shape of the central portion for 0° phase difference is a measure of relative amplitudes of the components. This slope is independent of delay difference as an inspection of Figure 19a confirms. More generally, the resultant slope in the overlap area is the algebraic sum of the component slopes. It is the algebraic difference, when the components are in phase opposition. For any intermediate phase, the resultant has the smaller slope, weighted by the cosine of the phase angle.

It is clear that three-component interaction complicates the effort of resolving individual parameters to an extent that makes it impractical. Based on the model calculations and meteorological measurements, two-component multipath propagation

is much more likely to occur. Similar observations can be made for sub-resolution effects on the AOA system. Because of the exponential gain function, effects are more difficult to interpret.

4. MULTIPATH DATA INTERPRETATION

Measurements were conducted on the Saddleback Mountain to Prospect Hill path on 74 days spanning the summer and fall months of 1983. Eleven of these days showed both multipath propagation and meteorologically verified ducting layers. The data of 1 November were selected for interpretation. Ducting activity on this particular day was significant. Table 1 and Figure 8 show, however, that it was not more significant than on the other four days listed. The radio data show great activity and variability during the meteorologically disturbed period of the day. But radio phenomena observed on 1 November were of the same scale as those on other days of multipath propagation. We therefore view 1 November as a typical, heavily disturbed day, well suited to compare modeling and simulation results with actually observed radio data. The presentation of 1 November data is preceded by test results of the TOA link undertaken earlier in order to demonstrate its expected performance.

4.1 Delay Resolution Test

On a day of a well-mixed atmosphere and no potential for multipath propagation we tested the performance of the TOA receiver for its delay resolution. While receiving a steady signal from the distant transmitter, we installed a T-section in the antenna to mixer waveguide. A length of waveguide was connected to the branching arm of the T and shorted at the far end. Two lengths of waveguide on hand produced 8-in. and 47-in. lengths of branch line between branch point and shorting plane. The specific lengths were arbitrary. With this configuration, a portion of the received signal traveling down the waveguide from the antenna is diverted into the branch line, another is reflected toward the antenna and lost, while the remainder continues on. Upon reflection at the end and return to the branch point, the branch line signal divides into one component following the original signal toward the mixer. Another travels back toward the antenna, and a third returns to the short to be reflected again. The subdivision of signals repeats continuously. We are interested in the sequence of signals traveling toward the mixer. Each subsequent one is delayed by the time it takes a signal to travel back and forth in the branch line. It is reduced in amplitude by a factor resulting from the division and from the attenuation in the guide. The amplitude ratio is constant between subsequent pairs of

echoes. With a free space wavelength $\lambda = 0.01894$ m and the inner width of the waveguide $a = 0.01576$ m, the wavelength λ_g within the air-filled guide follows from¹⁵

$$\lambda_g = \frac{\lambda}{\sqrt{1 - (\lambda/2a)^2}} = 0.02369 \text{ m.} \quad (11)$$

From this we can derive the phase velocity $v_{ph} = \lambda_s \cdot f = 3.753 \cdot 10^8$ m/sec and the group velocity $v_{gr} = c^2/v_{ph} = 2.398 \cdot 10^8$ m/sec with the free space velocity $c = 3 \cdot 10^8$ m/sec. The expected round trip time or echo delay in a branch line of length l is $\tau = 2l/v_{gr}$ or $\tau = 9.97$ nsec in a 47-in. line and $\tau = 1.69$ nsec in an 8-in. line.

Figure 20 shows stripchart recordings of actual measurements. Two 120-nsec delay scans of 6-sec length each present the no-multipath situation in (a), the 8-in. branchline effects in (b), and the 47-in. branchline effects in (c). Received power in dB is plotted with the calibration marked on the left ordinate. Part (a) shows the direct-signal main lobe and first sidelobe responses. Note the low level signals at greater delay range, mentioned earlier. We address Figure 20c next, where sufficient echo delay was introduced to make individual echoes clearly separable by the inherent delay resolution of the receiver. That is, essentially no signal phasing due to branchline echoes takes place in any of the sequential lobes displayed. In seven round trips the power level drops 31 dB or 4.4 dB/round trip. Also, seven round trips occur in 69.6 nsec or 9.94 nsec/round trip. This delay is in excellent agreement with the calculated quantity.

Echoes at 1.69 and 3.38 nsec with amplitudes of -4.4 and -8.8 dB are discernible on the downslope of the main signal response in Figure 20b. We did not establish the total phase shift imposed on the branch line signal accurately. From the narrowing of the main lobe near its top it appears that the first echo must have been nearly in phase opposition with the main signal. In that case, the second echo having accumulated twice the phase change is in phase again with the main signal. Figure 20b supports this reasoning. The overall decrease in signal level was not recognized at the time when the measurement was performed. The most likely explanation for it is a lossy connection.

15. Skolnik, M. (1970) Radar Handbook, McGraw Hill, New York:8-9.

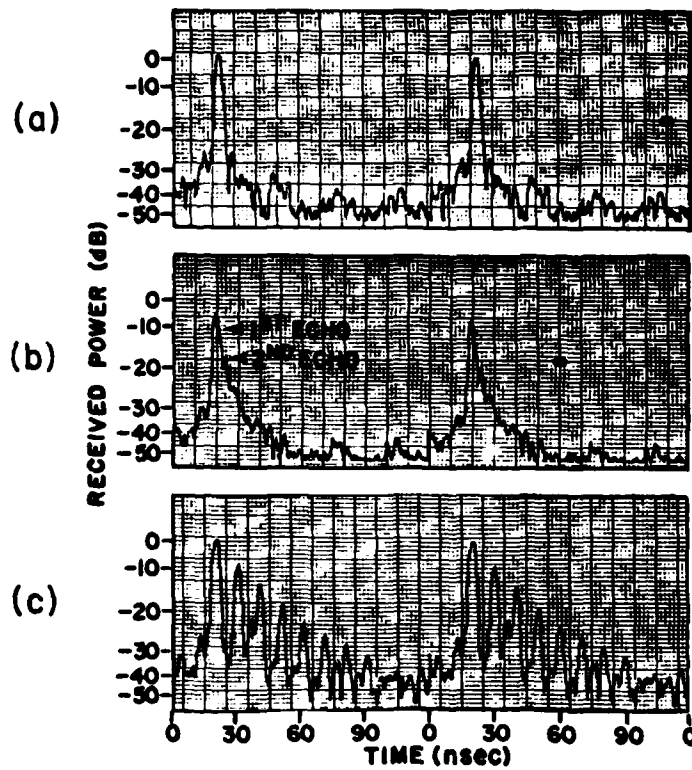


Figure 20. Experimental Delay Scans. (a) No atmospheric multipath, (b) 8-in. branch line in waveguide, and (c) 47-in. branch line in waveguide

4.2 Overview of 1 November 1983 Data

The radio data indicate that multipath activity on 1 November began on the previous evening. Lighter signal disturbances (in terms of fading depth) were found between 1800 and 0400. They continued in severe form throughout the morning until 0950. The angle of arrival measurements during the latter period are reproduced in Figure 21. The six 1-hr intervals arranged side-by-side overlap slightly. The antenna scans linearly between elevation angles of -0.7° and $+0.7^\circ$. One scan lasts 2.5 seconds. It is repeated every 6 seconds. Amplitudes are presented in logarithmic form with 0 dB the reference level under undisturbed propagation conditions. A cut-off level of -40 dB was chosen for the 3-D display. That is, signal levels below -40 dB are not shown for the benefit of a more illustrative display of higher level features. For comparison, meteorological data on this day exist between 0635 and 1030.

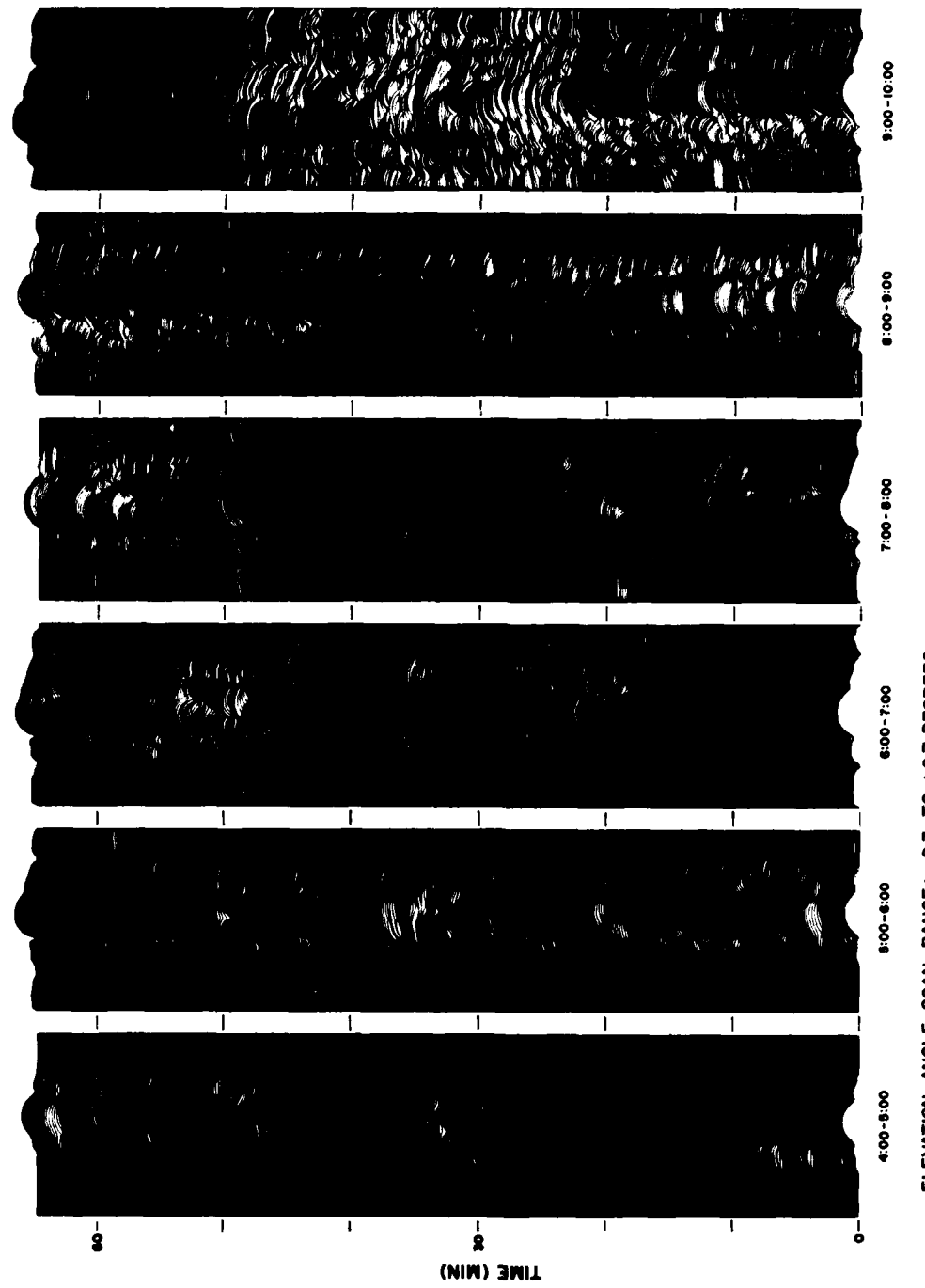


Figure 21. Received Signal Level vs Elevation Angle on 1 November 1983

It is evident in Figure 21 that the scan rate was sufficiently high during the multipath period to preserve most of the variations in the angle-of-arrival structure. Around 1000, conditions have normalized enough to show the undisturbed elevation beam pattern of the 29-ft antenna as it scans through the single signal arriving from the distant transmitter. The scan direction, upward from left to right, shows the upper sidelobes of the beam to the left of the main lobe, and the lower ones to the right. While the overall features of the beam pattern suggest that propagation has returned to normal, this is not yet the case on a more subtle scale. There is a low level roughness to the last two hours of scans that is in contrast with the smoothness seen on really disturbance-free days. Actually, much of the first four hours shows this smoothness if under severe multipath conditions. Compare the period from 0600 to 0610, where the beam features are essentially preserved with those from 0950 to 1000. We assume that this has to do with the scale of refractive irregularities. They are large during the early period but breaking up toward the end, when multipath propagation can no longer be sustained. Small scale signal fluctuations are thought to be the result of focussing and defocussing due to smaller irregularities which are in motion.

One outstanding feature in Figure 21 is the average change in main beam elevation angle. Although multipath components distort or destroy the main beam at times, its average location can be easily traced throughout the 6-hr interval. During the first hour the direct signal elevation angle lies between 0.01° and 0.03° . It rises slowly until at 0800 it is around 0.06° . At 0855 it reaches its high point of 0.08° and then goes down to 0.06° again at 0920. From here on it drops sharply by 0.24° in 15 to 20 minutes. Between 0940 and 1015 it stays at -0.18° . Under the assumption of a refractivity gradient of -40 N-units/km we expected the direct signal at -0.17° (see Figure 10; 0.05° added because of the layer tilt). Figure 10 also shows a 0.48° (0.05° added) angle of arrival if the ray were propagating through a uniform atmosphere of -300 N-units/km gradient. Plotting the elevation angle dependence on refractivity gradient from curves similar to Figure 10 one finds that they are directly proportional. Consequently, the highest bending observed on 1 November, leading to an arrival angle of 0.08° , can be interpreted as the effect of an average refractivity gradient of -142.4 N-units/km. This gradient is insufficient for ducting and hence multipath. It would explain relatively strong bending of only a single ray as seen around 0840. However, the atmosphere is known to be nonuniform with height, and the model shows that ducting may well be present over all or part of the height range to produce strong bending without multipath propagation.

The meteorological soundings on 1 November in Figure 8 illustrate the difficulty of reconciling the location and strength of measured ducting zones with the observed angle of arrival patterns. During the first, second, and third set of radio-sonde data, ducting gradient regions exist largely at receiver height (159.4 m)

and below. Only Hanscom AFB at 0635 and Salem at 0752 show ducting of moderate strength between receiver height and transmitter height (338.0 m). In the fourth and fifth set of soundings the regions of ducting gradient rise into and beyond this height range. There are some indications of the ducts sloping down in the V-shape mentioned earlier, but Deerfield measurements do not exist for confirmation.

The persistent positive angle of arrival at Prospect Hill during the period of meteorological probing demands strongly superrefractive conditions over the transmitter to receiver height range. Even the lowest average elevation angle of 0.01° corresponds to an effective refractivity gradient in that region of -115 N-units/km. Under superrefractive but non-ducting conditions the ray does not reach a height greater than the transmitter height. The measured refractivity changes between the transmitter and receiver heights and the average refractivity gradients are listed in Table 4.

Table 4. Refractivity Change and Refractivity Gradient Between Transmitter and Receiver Heights on 1 November 1983

Location	Time (h)	ΔN (N-units)	dN/dh (N-units/km)	AOA (deg)
Hanscom AFB	0635	22.7	-126.9	0.04
	0730	18.1	-101.2	-0.02
	0830	18.9	-105.6	-0.01
	0930	16.6	- 92.8	-0.05
	1030	10.1	- 56.5	-0.14
Salem	0642	17.5	- 97.8	-0.03
	0752	16.7	- 93.3	-0.04
	0826	15.5	- 86.6	-0.06
	0922	14.8	- 82.7	-0.07
	0946	13.2	- 73.8	-0.09

Assuming that the N-gradient is uniformly distributed in space, we have calculated the corresponding arrival angles for each case. The Hanscom AFB radiosonde data corroborate the radio data satisfactorily. The steep decline in angle of arrival between 0930 and 1030 does not repeat at Salem between 0922 and 0946, although the radio data suggest that the transition is accomplished by 0946. This discrepancy is somewhat surprising since the radiosonde should have recorded the overall drop in N accurately. Again, these measurements are localized and perhaps compensated for along the total path.

Signal amplitude development throughout the multipath events can be judged well on a short term scale. That is, variations within scans and between adjacent scans are obvious. Long term changes are less discernible in Figure 21 except indirectly by the presence or absence of specific sidelobes. Inspection of the concurrent stripchart recordings (an excerpt of AOA and TOA stripchart is shown in Figure 22) reveals minor amplitude fluctuations around the reference level at 0300. At about 0400 the peaks have slowly fallen to approximately -10 dB with valleys reaching to -30 dB. The maxima at 0713 and 0724 are at +5 dB. Another slow decrease results in peaks no higher than -10 dB around 0810. By 0910 the signal level has returned to normal. At 0933 and at 0938 it exceeds +12 dB. It slowly returns to normal by 1100 but is still near +6 dB at 1000, the end of the sequence shown.

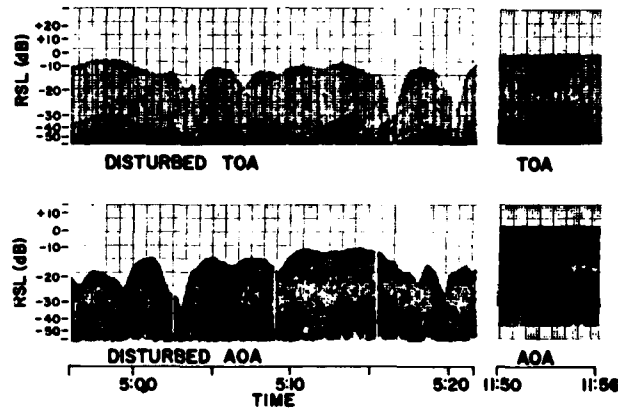


Figure 22. AOA and TOA Scan Amplitudes During and After Multipath Episode on 1 November 1983

While the quasi-periodicity is well recognizable in Figure 21, the stripchart discloses in addition that in the majority of cases, peak and valleys undergo gradual changes vs scan sequence. Some apparent notches, such as the one at 0520 in Figure 22, are not genuine notches but the crossover of lobes at two different angles, one increasing and the other decreasing in amplitude. This is contrary to the within-scan notches and only testifies to the comparatively slow phase changes between multipath components with time. A case in point is the well developed phasing null at 0549 which features two essentially equal component signals, not quite resolvable by the beam and similarly spaced above and below the expected main beam direction. Main beam phasing patterns take many different shapes throughout the 6-hr period. We will address specific cases in the next section.

Aside from the main lobe behavior, the sidelobes reveal structural developments of their own. Again, we will discuss specific situations such as those around 0715 and 0920 and their potential causes in the following section.

The breakup period of multipath conditions between 0920 and 0950 is a striking feature of Figure 21. During this interval, and particularly near 0935, the main beam location appears to fluctuate rapidly or even disappear. Scan resolution in this area is probably insufficient. We offer a qualitative explanation of observations by referring back to Figure 10. We know from Figure 8 and Table 4 that the gradient layer is rising and weakening. If the gradient in the ducting layer goes down, the question mark shape of the curve becomes less pronounced. The center portion leans less to the right until eventually it takes on a vertical slope, extending over a sizable range of angles before leaning left and not yielding multipath signals any longer. During the vertical-slope condition the arrival angle is highly susceptible to small disturbances in layer height. We do not claim that Parl's conditions prevailed exactly at the time, but presume a similar mechanism at work, resulting in unstable transitions between two stable conditions. Small disturbances then triggered the transitions.

The side-by-side display of AOA and TOA stripchart recordings in Figure 22 illustrates several interesting features. Each thin vertical line represents a quasi one-dimensional scan projection. The dwell time or number of passages of the pen at a specific amplitude level lends shading to the scan sequence which can be interpreted as structural information. The peak of each line is the highest level reached during a particular scan. Scans are not truly one-dimensional, since each scan is 2.5 sec (AOA) respectively 6 sec (TOA) long. The main lobes, however, cover only a fraction of the scan resulting in the line pattern. The signal maxima and minima of AOA and TOA scan sequences in Figure 22 are not well correlated for the most part. This is true of the whole multipath period. Uncorrelated fading on this link was expected due to the receiving antenna spacing.

The 3-D delay scan sequence in Figure 23, covering the period from 0400 to 1000, corresponds to Figure 21. Again, amplitudes are logarithmically compressed. Main lobe and sidelobe responses are shown as long as they exceed a level of -40 dB relative to the TOA reference signal under undisturbed propagation conditions. The abscissa, linear in relative delay, extends from 0 to 51.2 nsec. We mentioned earlier the marginal long term stability of the reference frequency sources. Because of this fact, the correlation peak of the signal will wander out of range under undisturbed propagation conditions if not corrected. The TOA receiver does this automatically by sensing the location of maximum output during each 48-bit scan. If the peak is not found at the 8th bit or 20 nsec into the scan, a correction of up to 4 bits is applied during the next scan. If the offset exceeds 4 bits, the maximum rate of correction is 4 bits/scan. This feature takes care of the clock instability

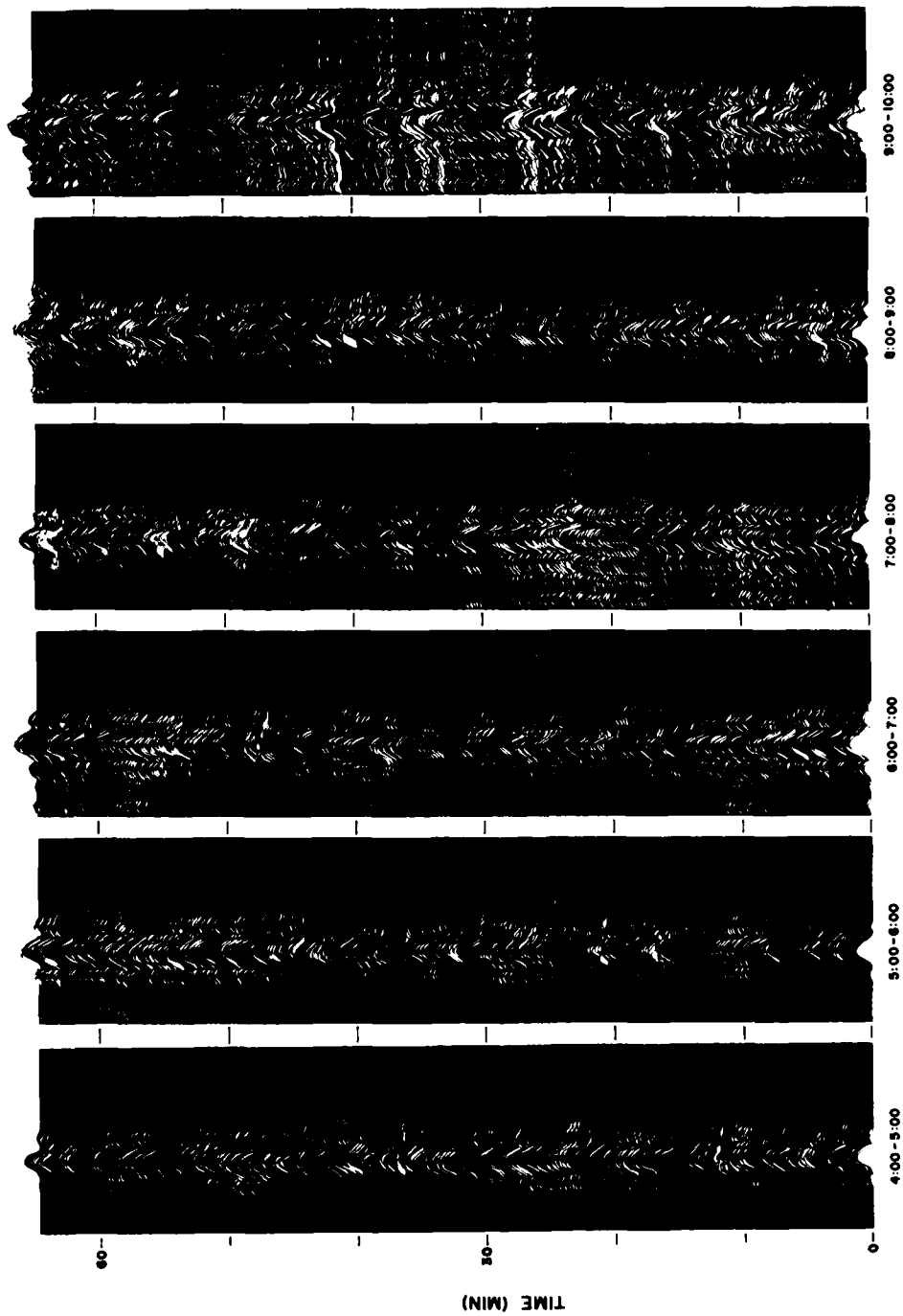


Figure 23. Received Signal Level vs Delay on 1 November 1983

problem, but complicates the interpretation of observed delay structure. In order for atmospheric multipath delays to be distinguishable from clock instability, they must occur on different scales. Through the observation of trends over a series of scans, this can often be accomplished. By the same token, if the original peak happens not to be the strongest any more under multipath conditions, the receiver will also correct for this situation.

No attempt has been made in Figure 23 to compensate for the receiver's corrective action. A close inspection reveals this on many occasions. For example between 0700 and 0710, an apparent systematic offset between the two reference frequencies is periodically compensated for by one-bit corrections. A larger single correction occurs at 0840. One-bit back-and-forth switching on successive scans like around 0720 is due to quantization uncertainty. The receiver realignments give the scan sequence a more ragged appearance throughout than in Figure 21. The overall change in signal level can be gauged by the appearance and disappearance of sidelobes and spurious responses at greater delays. The peculiarities of the raw-data plot make multipath effects more difficult to discern. Notwithstanding this fact, large scale multipath induced features that were so much in evidence in Figure 21 do not exist here. Sample sections of Figure 23 showing multipath episodes such as those around 0411 and 0445 will be enlarged later and discussed in detail.

4.3 Multipath Angular Events

Figure 21 presents a time period disturbed by a variety of multipath interference patterns. These are produced by a number of variables interacting simultaneously, the variables including number of rays, their amplitudes, angles of arrival and phases. To study the effect of a specific parameter independently regions were sought which might be closely simulated by varying that parameter only. The following three cases will be examined (there are two variables in the second case): Figure 24 is largely dependent on amplitude variation. Figure 25 shows the effect of both angle of arrival and phase changes. In Figure 26 phase change is the predominant cause of the observed scan pattern. Amplitude scales of measured and simulated events are comparable but not identical.

The most prominent feature in Figure 24a is the double-peak pattern which exists over the central area of the scan sequence. Note the rather abrupt reduction and subsequent more gradual increase in overall amplitude during this double-peak event, an effect especially evident in the sidelobes. This is accompanied by an abrupt leftward shift and subsequent more gradual rightward shift of the double peaks. At the beginning of the event the main peak is seen to drop in amplitude and drift slightly leftward while, at the same time, the right peak establishes itself,

grows in amplitude and drifts to the left as well. Shortly after the secondary peak surpasses the main peak in amplitude, the process reverses. The main peak's amplitude gradually returns to normal and its central position is re-established as the secondary peak recedes.

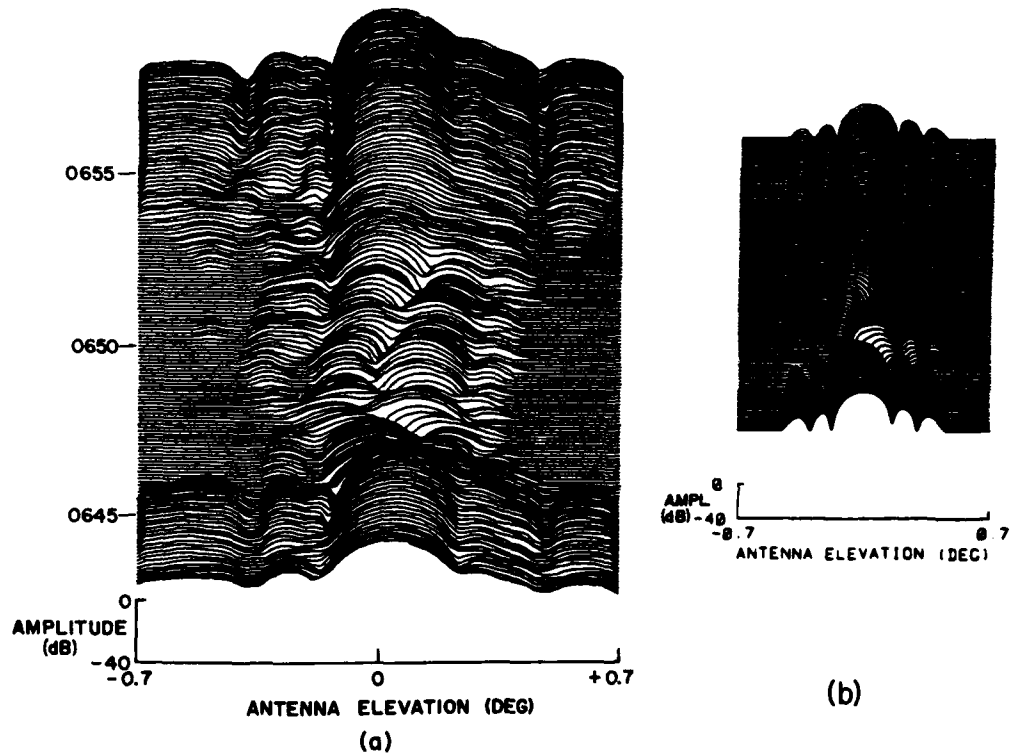


Figure 24. AOA Scan Sequence on 1 November 1983 Based on Amplitude Change, (a) Measurement, (b) Simulation: $A_1 = 2$, $\phi_1 = 0^\circ$, $\beta_1 = 0^\circ$; $A_2 = 0.4$, $\Delta A_2 = 0.06/\text{scan}$ (scans 1-30), $\Delta A_2 = -0.015/\text{scan}$ (scans 31-100), $\phi_2 = 180^\circ$, $\beta_2 = 0.005^\circ$

In the simulation of this event (Figure 24b) it is interesting to note the simple conditions needed to produce strikingly similar effects. The figure caption lists the amplitude, phase, and arrival angle for each component plus the rate of change for these parameters. One additional component ray is required which is out of phase with the main ray and which is only slightly offset from it in angle. The only variable in the process is the amplitude of the multipath ray. In this case it starts out very small, grows to a level 10 percent greater than that of the main ray and slowly

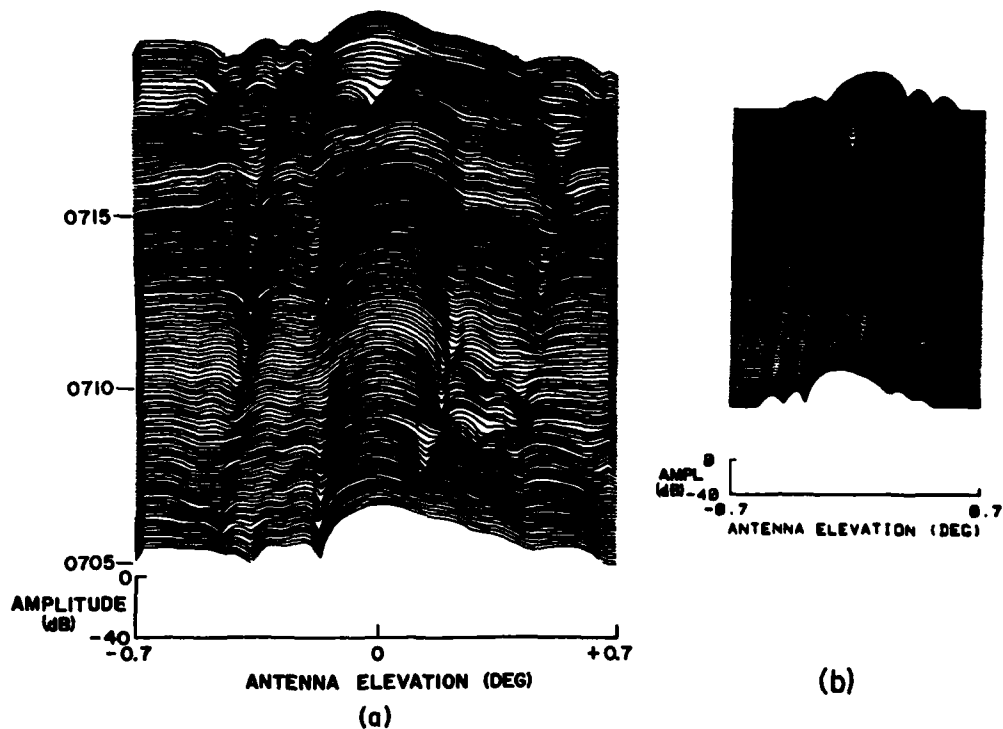


Figure 25. AOA Scan Sequence on 1 November 1983 Based on Phase and Angle Changes, (a) Measurement, (b) Simulation: $A_1 = 0.06$, $\phi_1 = 0$, $\beta_1 = 0$, $A_2 = 1.2$, $\phi_2 = 270^\circ$, $\Delta\phi_2 = -5.625^\circ/\text{scan}$, $\beta_2 = -0.1^\circ$, $\Delta\beta_2 = 0.002^\circ/\text{scan}$

diminishes to negligible size. It is of particular interest that the apparent angular drift in the pattern is not due to any actual change in angle of arrival but due to an out-of-phase component ray which is slightly offset from the main ray in angle.

Noteworthy characteristics of the scan sequence in Figure 25a are: (1) the phasing nulls in the main lobe on the right side of scans near the beginning and on the left side near the end of the event, (2) the subtle impression (especially in the sidelobes) of an underlying component with an overall left-to-right angular drift, and (3) the bulge in amplitude across the entire waveform in the central area of the plot. This case can also be simulated quite closely (Figure 25b) with two rays. Ray 1 is again the fixed reference ray with the parameters as given in the caption. Ray 2 has a constant amplitude throughout the sequence. However, the phase of ray 2 is allowed to change with each successive scan. Simultaneously, the angle of arrival increases systematically. The resulting picture has the general appearance of the measured pattern with the following to be pointed out. Both the data plot and the simulation display a reinforcement peak near the center of the event though the pattern

is otherwise undisturbed. Here the arrival angle and phase of ray 2 equal those of ray 1 and the rays just add. Toward the end of the event the main lobe shows a notch caused by ray 2 being out of phase and offset in angle by about 0.05° . The leftward position of the notch is due to ray 2 (the right hand component) being of greater amplitude than ray 1, an effect pointed out in the previous case. Accordingly, near the beginning of the sequence where ray 2 is slightly on the left of ray 1 and 180° out of phase, the notch appears on the right side. Similarities can also be seen in the more subtle detail of the sidelobes, most notably how the valleys between sidelobes shift laterally and how some sidelobes seem to disappear into valleys while others grow out of them. This area of the data might then be considered a case where the progressing phase change of 360° between notches in 10 to 12 min is accompanied by approximately 0.1° of angle change over the same duration.

The effects to be examined in Figure 26a are (1) the fairly rapid angular drift of the sidelobes on the lower left side of the plot and the recurrent, cyclic nature of this drift, while (2) the main lobe is relatively unaffected in this region. The drift itself suggests a change in angle of arrival of a multipath ray. However, the repetitive nature of the pattern is hard to explain by angular motion. The sidelobe motion in this case is not accompanied by a similar motion in the main lobe. This suggests that the multipath component's main lobe is of comparable amplitude and located near the upper sidelobes of ray 1. Such conditions explain why other areas of the pattern show no significant interaction. If the interfering ray 2 is assumed to arrive at an angle between the main lobe and first sidelobe of ray 1, the interaction between ray 1 and 2 would yield notches in the main lobe of ray 1, a result which the data do not show (unlike the previous two cases). On the other hand, if ray 2 arrives at an angle between the first and second sidelobes of ray 1, the apparent sidelobe drift can be simulated without causing main lobe dimpling. Since the first sidelobe is 0.22° away from the main lobe, this means that the multipath ray must have arrived more than 0.22° lower than the direct ray. The angle of arrival of the direct ray is 0.06° during this period. The multipath ray must therefore come in at -0.16° elevation or below. Referring back to Figure 7b we see that this is conceivable. That is, extrapolating for $k > 1.4$, the required multipath signal may still be of atmospheric origin and not due to terrain reflection at Walnut Hill. However, the latter possibility cannot be ruled out, considering the low amplitude of this ray.

Actually, the simulation (Figure 26b) assumes a dual co-located ray at an elevation angle of -0.28° . Both signals are of equal amplitude. One is in phase quadrature with the direct signal and the other advances in phase at 18° per scan. This configuration is in agreement with model predictions in Figures 10 and 11. When dual rays first occur their phase difference grows with no substantial angular

separation. Figure 26a shows the shell-shaped periodic structures associated with the inner sidelobe sloping toward the main lobe as in the simulation. The outer sidelobe, fading periodically, has no lateral motion. A close inspection of Figure 21 reveals similar structures throughout the morning.

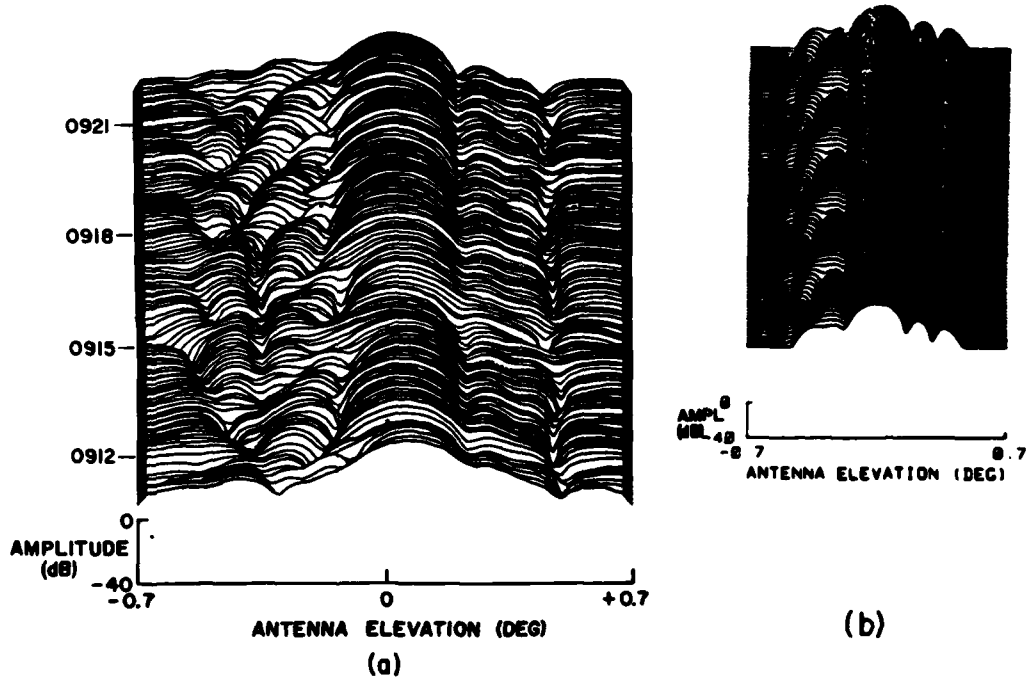


Figure 26. AOA Scan Sequence on 1 November 1983 Based on Phase Change, (a) Measurement, (b) Simulation: $A_1 = 0.8$, $\phi_1 = 0$, $\beta_1 = 0$, $A_2 = 0.1$, $\phi_2 = 0$, $\Delta\phi_2 = 18^\circ/\text{scan}$, $\beta_2 = -0.28^\circ$, $A_3 = 0.1$, $\phi_3 = 90^\circ$, $\beta_3 = -0.28^\circ$

4.4 Multipath Delay Events

Two episodes of apparent multipath propagation were selected from Figure 23 for a more detailed discussion. The left scan sequences of Figures 27a and 28a are enlarged reproductions of the raw data in Figure 23. They exhibit the scan range adjustments explained earlier. Only the 5 to 35-nsec portion is shown. In part (b) of the two figures a sequence of 15 scans from the most active area in part (a) is spread apart further to avoid overlap between traces. In addition, alignment steps were removed which obviously disturbed the natural progression of scans. Part (c) is a simulation of the expanded, active area.

In Figure 27b the main correlation peak is seen to broaden on the left when an in-phase secondary component appears. As time proceeds, the main peak diminishes, the secondary peak grows, and a phase shift between the two accumulates. A notch gradually appears between the two as they approach similar amplitudes and phase opposition. The secondary peak continues to grow in amplitude as the main peak fades. The net result is a takeover by the secondary ray in scan 13 from the bottom. The two components do not seem to undergo substantial delay changes. However, this cannot be said with certainty because of a potential compensating drift in the time reference frame. It can be said that the secondary peak which becomes dominant, precedes rather than follows the main peak.

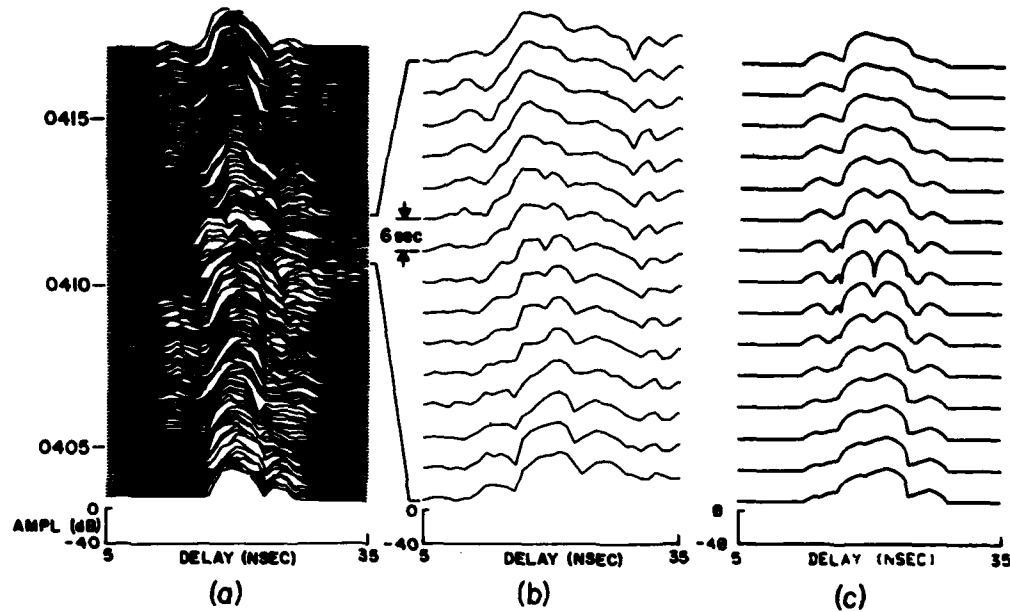


Figure 27. TOA Scan Sequence on 1 November 1983 Based on Two-Component Multipath, (a) Measurement, (b) Expanded Measurement, (c) Simulation:
 $A_1 = 1$, $\Delta A_1 = -0.04/\text{scan}$, $\tau_1 = 0 \text{ nsec}$, $A_2 = 0.4$, $\Delta A_2 = 0.04$,
 $\tau_2 = -2.966 \text{ nsec}$, $\Delta \tau_2 = 0.0045 \text{ nsec/scan}$

In accordance with the findings on sub-resolution effects in Section 3.4 we observe the following. The scans of Figure 27b agree in their quarter-bit step width with those simulated in Figure 19a. Figure 27b has a logarithmic amplitude scale. Hence, a less pointed appearance must be expected here. None of the simulated cases for a relative component delay of less than one bit (0 through 3τ) show a

composite peak spacing of more than one bit. The same holds for other amplitude ratios between 0 and 2 investigated but not shown in Figure 19a. The composite peak spacing in Figure 27b is 3 nsec on average. Based on the bit width of 2.5 nsec and the simulations for composite peak spacing between one and two bit widths (4τ through 8τ), the two peaks visible during part of the scan sequence represent the true peaks of the component signals. The relative delay between components changes insignificantly while the two peaks are recognizable. For a 180° phase shift a change in delay difference of only 0.04 nsec is required. This is indiscernible on the delay axis.

Both component amplitudes are nearly equal during the eighth and ninth scan. For equal amplitude components a scan sequence as in Figure 19a shows flat topped peaks. There are indications of flat tops in the data. Perfect phase opposition between two interfering components is expected to lead to complete cancellation at some point in the composite waveform. There is only partial cancellation in Figure 27b. This is due to the fact that scan and phasing null did not occur at the same instant.

The simulation in Figure 27c assumes two signals, one increasing and one decreasing in amplitude. The delay difference of 2.966 nsec translates into an in-phase condition during the first scan at the 15.84-GHz carrier frequency. The change rate of delay difference was chosen for the deepest notch to coincide with that in the measured pattern. Similarities can be observed in the sidelobe structure.

Figure 28 is an example of the presence of three multipath rays. The larger, secondary ray is seen to broaden the right side of the main ray, increase in amplitude and cause a phase notch between the two in a manner similar to the previous case. The secondary ray, however, diminishes subsequently and does not take over as in the previous case. Also, the secondary ray is on the right side of the main ray instead of the left. The other interfering ray, number 3, is to the right of ray 2 and grows continuously through the event. It appears that the first 10 or 11 scans in Figure 28b represent a gradual phase change between the main ray and its nearby interfering ray of 180° or less. The development starts essentially in phase and is out of phase where the deepest notch results. Again, the delay change of 0.03 nsec required for this is too small to show on the delay axis.

The interpretation above implies that the three components are resolved by the TOA receiver and the observed peaks are at the true delays of individual components. This is likely the case between rays 1 and 2 but questionable between rays 2 and 3. Consulting Figure 19a we find within the 0 to 1-bit delay range and the reference signal of higher amplitude than the delayed one, that the location of the reference peak is preserved both in the sum and difference pattern. Its amplitude changes with the delayed component's spacing. We investigated this result for other amplitude ratios and found it to be generally true. The measured delay between

rays 1 and 2 is therefore equal to 2.8 nsec. Unfortunately no conclusions can be drawn from Figure 28b as to location and amplitude of the third component. With the third component's amplitude obviously much lower than that of the second, the apparent peak is spaced one bit width delayed from the second component. The true location of the third component can be anywhere in between.

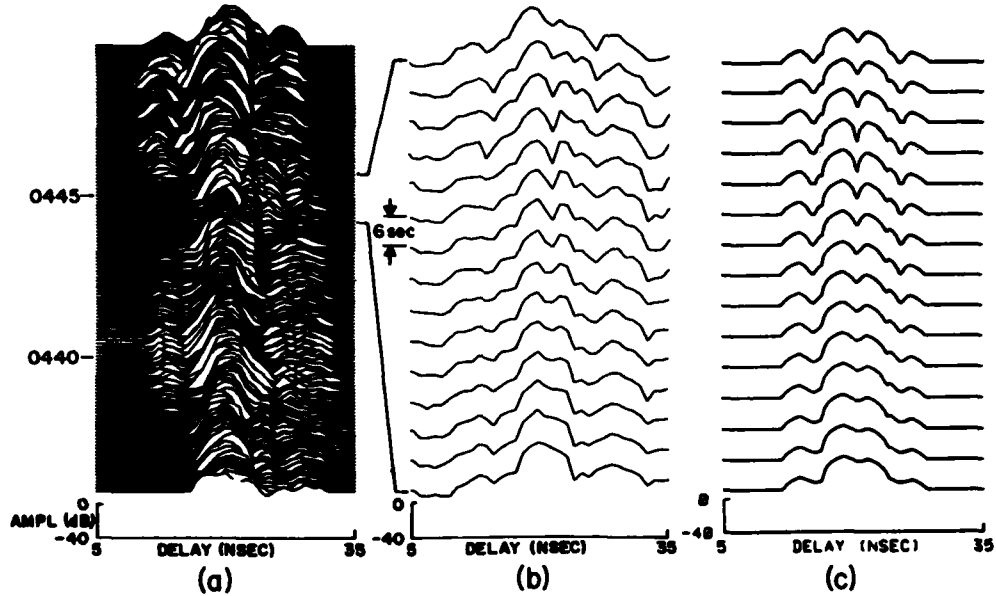


Figure 28. TOA Scan Sequence on 1 November 1983 Based on Three-Component Multipath. (a) Measurement, (b) Expanded Measurement, (c) Simulation:
 $A_1 = 1$, $\tau_1 = 0$ nsec, $A_2 = 0.7$, $\tau_2 = 2.794$ nsec, $\Delta\tau_2 = 0.0015$ nsec/scan,
 $A_3 = 0.05$, $\Delta A_3 = 0.004$, $\tau_3 = 4.016$ nsec, $\Delta\tau_3 = 0.003$ nsec/scan

With these caveats in mind, the simulation in Figure 28c is also based on three components. The first and second rays are of constant amplitude while the third grows with scan number. Initial delay differences are chosen such that they approximately match the ones read from the measured scans. The third component's delay is compatible with the findings in Figure 19. Exact values as well as change rates per scan are determined by the best apparent match between measurement and simulation.

5. CONCLUSIONS

The interrelation between meteorological and radio phenomena under atmospheric multipath conditions has been studied on a long terrestrial line-of-sight link. Ray bending due to refractivity gradients is well understood. Theoretically, radio parameters can be calculated if the spatial refractivity structure is known. Conversely, a model of the propagation medium can be reconstructed from the radio parameters. In practice, neither meteorological nor radio parameters are known with sufficient accuracy to achieve one or the other objective by itself in a satisfactory manner. We have therefore approached the problem from several directions including meteorological measurements, radio measurements, propagation modeling and radio data simulation.

Soundings of the refractivity structure are by necessity sparse in time and space. This is justified to a degree by the assumption that on a scale representative of terrestrial line-of-sight paths the lower atmosphere is predominantly structured in the vertical direction. Variations occur slowly. Modeling of the mechanism tells us that whatever the variability of refractivity along the path, there must be an effective stratification over much of it to bring about multipath propagation under typically measured refractivity gradients. Besides, modeling calls for a slope to the stratified structure to compensate for path inclination. This reduces the effective height difference between terminals and again is required to produce multipath propagation under the observed conditions.

Ducting regions are of limited thickness and are imbedded in superrefractive structures of wider extent. It is likely that the meteorological sensors measure the average superrefractive structure more faithfully than the narrow ducting regions. The simple model assumption of a ducting halfspace on top of a non-ducting one serves to answer many qualitative questions as to how atmospheric multipath comes about. Its insufficiency in representing the true conditions is most apparent, when addressing experimental radio signal changes over minutes or tens of minutes. They are incompatible with the rigid large scale model layer which is allowed to move in altitude as a whole. In terms of the model, boundary height is critical to the multipath situation. It is unlikely that there is such a well defined boundary in the real world, moving in a concerted fashion to produce the signal changes observed. Judging from the radio data, the whole region between the transmitter and receiver probably possesses superrefractive gradients substantially above normal with patches of ducting strength interspersed. These patches are more mobile and variable in strength than the overall structure, creating multipath scenarios compatible with the radio observations. At the same time they are difficult to detect meteorologically and to associate with spaced soundings. Notwithstanding these

complications, the ranges of observed angles of arrival and delays do agree with the model predictions.

The simulations of radio system outputs with assumed wave parameters provide a valuable link between measurement and theory. They benefit the resolution obtainable with our angle and delay sensing instrumentation. A convincing connection between the model and the simulation is difficult to make. The reason is that the model is not capable of handling a more realistic meteorological structure, nor are we in a position to provide one in sufficient detail and temporal development, to expect replica of the radio data to come out of the simulation. One simulation tied to the rigid output from the model was presented here, assuming a steadily rising ducting layer. The model case simulation provides insights into features seen during angle and delay scans. However, no multipath episode was probed experimentally that followed the model case to a large extent.

The strength of the simulation programs is that they allow a free choice of wave parameters that fit actually observed scan developments. The results, if convincing, are necessarily implications. It is possible that a different set of wave parameters results in a similar scan development.

This report has essentially been a presentation of the experimental systems and a development and description of the analytical tools for data interpretation. Their applicability is demonstrated in a case study. Further results from this program will follow.

References

1. Monsen, P. (1980) Fading channel communications, IEEE Comm. Magazine, January:16-25.
2. Parl, S., and Malaga, A. (1984) Theoretical Analysis of Microwave Propagation, RADC-TR-84-74, AD A 143762.
3. Webster, A. R. (1982) Angle of arrival considerations in microwave communications systems, IEEE Trans. on Ant. and Prop., AP-30(No. 4):800-802.
4. Ruthroff, C. L. (1971) Multi-path fading on line-of-sight microwave radio systems as a function of path length and frequency, Bell Sys. Tech. J. 50(No. 7):2375-2398.
5. Parl, S. (1983) Characterization of multipath parameters for line-of-sight microwave propagation, IEEE Trans. on Ant. and Prop. AP-31(No. 6):938-948.
6. Sasaki, O., and Akiyama, T. (1979) Multipath delay characteristics on line-of-sight microwave radio system, IEEE Trans. on Comm. COM-27(No. 12):1876-1886.
7. CCIR International Radio Consultation Committee (1982) Recommendations and Reports of the CCIR, Vol. V (Prop. in Non-Ionized Media) Geneva, 1982.
8. Livingstone, D. C. (1970) The Physics of Microwave Propagation, Prentice-Hall, Englewood Cliffs, New Jersey:33.
9. Barton, I. J. (1973) The importance of tilted layers in the tropospheric ducting of radio waves over the Timor Sea, Radio Sci. 8(No. 8, 9):727-732.
10. Schleher, J. S. (1982) Tilted refractive surfaces at Eglin Air Force Base, Florida, Radio Sci. 17(No. 5):1281-1284.
11. Izumi, Y., and Morrissey, J. F. (1982) Meteorological Measurements on the Monadnock-Prospect Hill Communication Link, AF Geophys. Lab. unpublished report.
12. Kerr, D. E. (1951) Propagation of Short Radio Waves, Rad. Lab. Ser. Vol. 13, McGraw-Hill, New York:263.

References

13. Rummel, W. D. (1979) A new selective fading model: application to propagation data, Bell Syst. Tech. J., 58(No. 15):1037-1071.
14. Pickering, L. W., and DeRosa, J. K. (1979) Refractive multipath model for line-of-sight microwave relay links, IEEE Trans. on Comm. COM-27(No. 8):1174-1182.
15. Skolnik, M. (1970) Radar Handbook, McGraw-Hill, New York:8-9.

MISSION of Rome Air Development Center

RADC plans and executes research, development, test and selected acquisition programs in support of Command, Control, Communications and Intelligence (C³I) activities. Technical and engineering support within areas of competence is provided to ESD Program Offices (POs) and other ESD elements to perform effective acquisition of C³I systems. The areas of technical competence include communications, command and control, battle management, information processing, surveillance sensors, intelligence data collection and handling, solid state sciences, electromagnetics, and propagation, and electronic, maintainability, and compatibility.

END

FILMED

11-85

DTIC